Benemérita Universidad Autónoma de Puebla

Facultad de Ciencias Físico Matemáticas

Estudio de modos de superficie plasmónicos en multicapas basadas en materiales bidimensionales

Tesis presentada al

Posgrado en Física Aplicada

como requisito parcial para la obtención del grado de

Maestro en Ciencias

por

Edgar Efrén Tomay Tiburcio

Asesorado por

Dr. Iván Fuentecilla Cárcamo

Dra. Martha Alicia Palomino Ovando

Puebla Pue.
Diciembre 2024

Benemérita Universidad Autónoma de Puebla

Facultad de Ciencias Físico Matemáticas

Estudio de modos de superficie plasmónicos en multicapas basadas en materiales bidimensionales

Tesis presentada al

Posgrado en Física Aplicada

como requisito parcial para la obtención del grado de

Maestro en Ciencias

por

Edgar Efrén Tomay Tiburcio

Asesorado por

Dr. Iván Fuentecilla Cárcamo

Dra. Martha Alicia Palomino Ovando

Puebla Pue.
Diciembre 2024

Título: Estudio de modos de superficie plasmónicos en multicapas basadas en materiales bidimensionales
Estudiante: Edgar Efrén Tomay Tiburcio

COMITÉ

Dra. Claudia Oliva Mendoza Barrera
Presidente

Dr. José Alejandro Hernández López
Secretario

Dr. Gregorio Hernández Cocoletzi
Vocal Externo

Dr. Víctor Manuel Altuzar Aguilar
Suplente

Dr. Iván Fuentecilla Cárcamo
Asesor

Dra. Martha Alicia Palomino Ovando
Asesora

Ella dijo que se iría
y que se llevaría todo lo que era suyo.
Ella se fue. Y no me llevó a mi.
Y yo era suyo.

Acknowledgments

Esta tesis representa la culminación de dos años competitivos en mi formación académíca como físico, pero también la consolidación y satisfacción personal de un sueño que comenzó hace muchos años en un modesto salón de clases de primaria. Quiero agradecer en este espacio a todos aquellos seres que me han demostrado que nunca se está sólo en el camino. En primera instancia, quiero hacer mención de las personas que me han enseñado lo complicada y valiosa que es la vida, mis padres, *Francisco* y *Rosalina*; y a mis hermanos, *Emmanuel* y *Uriel*. Gracias por su apoyo, su lealtad, su comprensión, su tolerancia, sus consejos, por todo.

A mis amigos, siempre estaré dispuesto a apoyarlos sin importar el tiempo ni la distancia, como ya ustedes me lo han demostrado. *Elizabeth*, *Miguel*, *Gabriel* y *Julio* por aquellos episodios tan divertidos que hemos compartidos desde la preparatoria, por acompañarme en momentos díffíciles y ser como esa bella inspiracion que todo poema necesita. A mis amigos de la FCFM: *Jorge*, *Mariana*, *Marco* y *Boggart*. A mis asesores, *Dr. Iván Fuentecilla Cárcamo* y *Dra. Martha Alicia Palomino Ovando*, por guiarme en este camino y su paciencia al transmitir conocimientos. Gracias a ti, alcanzamos una meta más y estaremos preparados para lo que venga. *Hacia tantos años que no alzaba la cara que me olvidé del cielo... está tan alto.*

¡Gracias totales!

Contents

List of Figures

List of Tables

Summary

The purpose of this thesis was to analyze the optical properties of graphene and phosphorene configurations, examining their diverse potential applications as plasmonic support media. Graphene, a two-dimensional allotrope of carbon, has emerged as a revolutionary material due to its hexagonal structure, exceptional conductivity, lightweight nature and mechanical strength. On the other hand, black phosphorus is a layered semiconductor with a *corrugated* hexagonal structure in each monolayer (called phosphorene) that has garnered attention within the scientific community as a potential candidate for studying surface plasmons. This study focuses on analyzing the optical properties of photonic crystals based on graphene or phosphorene in terms of band formation and plasmonic mode coupling.

Keywords: *Plasmons, Two-dimensional materials, graphene, phosphorene.*

Introduction

Graphene is a two-dimensional material composed of an hexagonal tessellation of carbon atoms, was first materialized in 2004 through the ingenuity of A. Geim and K. Novoselov using the innovative technique of mechanical exfoliation, followed by careful transfer to a silicon substrate [1]. This milestone marked a paradigm shift in materials technology, challenging the previous notion of the impracticality of 2D materials due to their supposed instability. Furthermore, the synthesis of these two-dimensional materials has not only been revolutionary in itself but has also triggered a spectrum of applications in the fields of electronic and optoelectronic devices, meeting the demands for low-dimensionality and energy efficiency. Also, doped graphene has revealed the existence of plasmonic modes with transverse magnetic polarization (TM) in the Terahertz range and transverse electric (TE) in the far-infrared range, where inter-band transitions predominate [2].

Following the creation of graphene, various two-dimensional materials have been synthesized, including transition metal dichalcogenides (TMDs), hexagonal boron nitride, gallium nitride, and others, using the mechanical exfoliation technique [3]. A notable achievement occurred in 2014 when phosphorene, a two-dimensional layer composed of phosphorus atoms arranged in a corrugated 2D lattice, was synthesized using the same technique. Unlike graphene, phosphorene derived from black phosphorus exhibits semiconductor properties with a tunable band gap ranging from 0.3 eV to 2 eV [4]. Due to its semiconductor properties, phosphorene presents itself as a promising option for applications in electronics, optoelectronics, thermoelectricity, and nanotechnology in general, contributing to the development of field-effect transistors, photodetectors, sensors and flexible low-dimensional optoelectronic devices [5, 6]. Moreover, doped phosphorene has been demonstrated to support surface plasmons, offering the possibility of tuning them along the principal directions (*armchair* and *zigzag*) due to the electric field effect. Excitation of these plasmonic modes can be achieved through various techniques such as diffraction gratings, near-field optical microscopy, and attenuated total reflection (ATR), among others [7].

Since periodic graphene-based structures have demonstrated the coupling of surface plasmon modes and band formation (phenomena observed in both polarizations [8]), and considering the conducting properties of doped phosphorene, it is anticipated that surface plasmonic modes in phosphorene can uniquely interact when placing phosphorene layers close to each other. In the Terahertz regime, the optical properties of phosphorene can be modeled using Drude-like conductivity with two principal directions along the *armchair* and *zigzag* directions. This suggests the potential formation of plasmonic bands with TM polarization in the same frequency range. It is worth noting that, in both cases, surface plasmonic modes are tunable via electrical doping techniques, meaning the phenomena observed in phosphorene-based structures derived from surface plasmonic modes are externally adjustable. In this work, we analyze the perspective and behavior of analogous phenomena already observed in graphene-based and phosphorene-based structures, which open up a broad field of research and development in two-dimensional material science and envisioned innovative technological applications.

Chapter 1

Two-dimensional Materials: Graphene and phosphorene

In this chapter, the general properties of two-dimensional materials are reviewed in terms of their remarkable properties; researchers have since broadened their focus to include an array of materials spanning the periodic table. This expansion has been fueled by the quest for materials with tailored electronic characteristics suitable for diverse applications. The manipulation of two-dimensional materials through various techniques offers unprecedented opportunities in science. We focus this chapter on two specific 2D materials: graphene and phosphorene, therefore exploring some of the most significant characteristics for both.

1.1 Two-dimensional materials.

The science of two-dimensional materials could arguably be said to have begun with the first successful exfoliation of graphene in 2004 [1], which has since been the subject of countless investigations driven by its thin thickness, promising for electronic device miniaturization. Additionally, carrier confinement to the plane imparts unique and extraordinary physical properties such as high carrier mobility, electrical and thermal conductivity, and remarkable transparency. These properties generated high expectations around graphene, initially considering it as an ideal silicon substitute. However, its lack of a bandgap limits its efficiency in electronic and optoelectronic applications. Nevertheless, this fact spurred the fabrication of new two-dimensional (2D) materials, now encompassing a wide range of elements from the periodic table, offering varied electronic characteristics, including metals, semi-metals, insulators, and semiconductors with direct or indirect bandgaps. Some studies have named these materials as *van der Waals materials* because layered materials are characterized by planar structures held together by weak out-of-plane van der Waals forces [3]. Fig. (**1.1**) shows a diagram of some layered materials expanding in the spectrum of their electronic properties, including semiconductors, insulators, semi-metals, metals and/or superconductors.

Today, the number of research studies related to 2D materials is steadily growing, thanks to their intrinsic properties and the ease of adjusting them (e.g. electron mobility and magnetic properties). This adjustment can be achieved through various approaches, such as layer number, doping level, external field tuning, and the creation of heterostructures. This modulation of 2D materials offers a wide range of properties with exceptional performance, positioning this family at high potential in nanoelectronics, optoelectronics, as well as numerous technological applications.

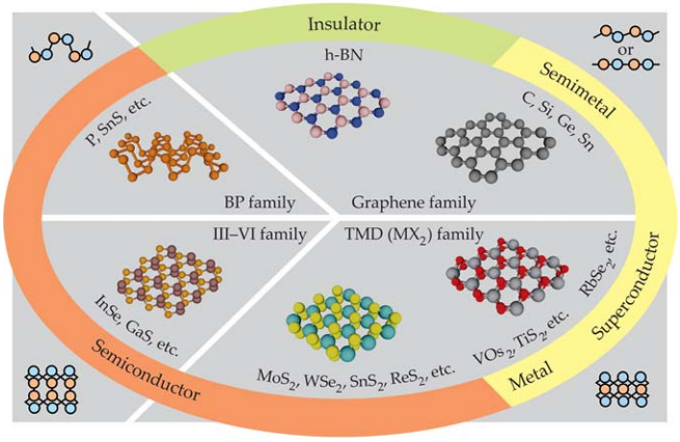

Figure **1.1**: Some examples of two-dimensional materials (such as graphene, black phosphorus and TMDs) classified into four families depending on their electronic properties. Diagram taken from [3].

1.2 Graphene.

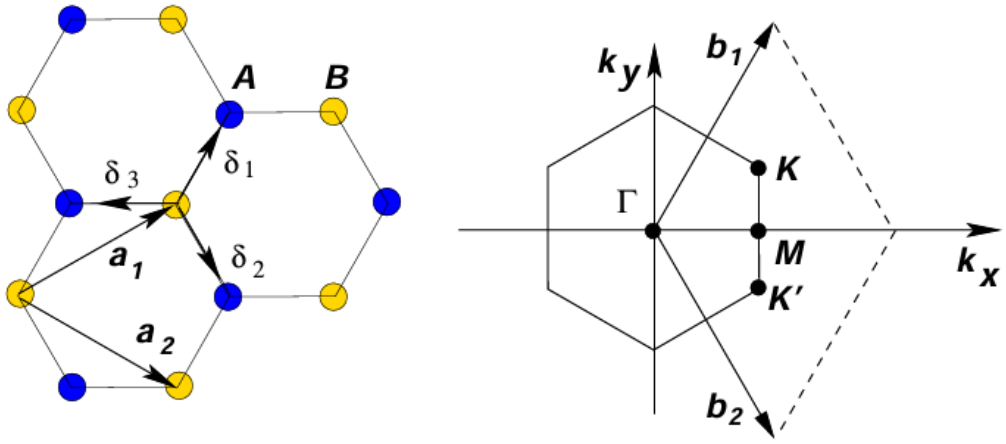

Figure **2.2**: Left: Atomic structure of graphene. Right: Brillouin Zone with its K-points. Diagrams taken from [2].

Graphene, a flat monoatomic sheet of carbon atoms bonded together by covalent bonds (fig. **2.2**) has been the subject of theoretical study within various research for decades, although its existence as an isolated entity was considered impossible due to the supposed thermodynamic instability of strictly two-dimensional crystals. This instability was attributed to divergent contributions from thermal fluctuations in low-dimensional crystal networks, theoretically causing atomic displacements comparable to inter-atomic distances at finite temperatures. Numerous experimental proofs supported this hypothesis, including the discovery that the melting temperature of thin sheets decreases rapidly as their thickness is reduced, becoming unstable for thicknesses close to a dozen monolayers. This generally led two-dimensional crystals to adopt various three-dimensional structures to gain stability at the expense of losing their two-dimensionality [1].

However, as already mentioned in the Introduction, in 2004, a group of scientists led by A.K. Geim and K.S. Novoselov succeeded in obtaining and identifying individual graphene layers, along

with other two-dimensional crystals. Because of its exceptional physical properties, graphene is considered a standout material in both fundamental physics research and practical applications. Electronically, graphene is a special case of a semi-metal with a zero bandgap similar to that of metals. However, its density of states (DOS) at the Fermi level is zero, similar to semiconductors [2]. Its electronic band structure exhibits linear dispersion with respect to momentum for low energies, akin to the Dirac equation for massless fermions, making graphene a two-dimensional system of massless Dirac fermions (fig. **2.3**).

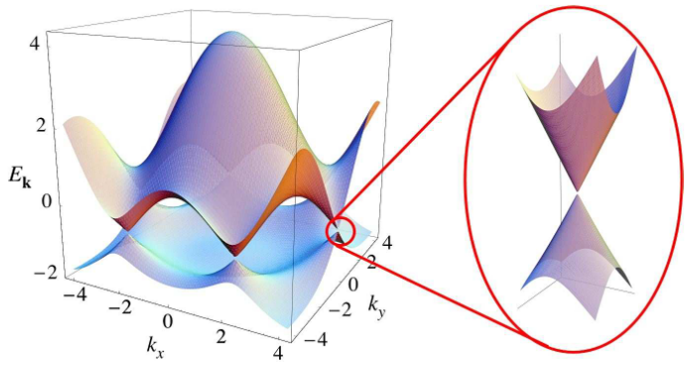

Figure **2.3**: Energy band spectrum at the K-points for graphene.

In general terms, graphene has proven to be an extraordinary material with diverse characteristics and potential applications, as mentioned earlier. Undoubtedly, it is a precursor in the study and application of 2D materials, giving rise to new lines of research in obtaining and implementing these materials. This not only revolutionizes the way technology is made and applied but also establishes connections with other fields of study in physics, contributing to both technological advancements and frontier science understanding.

1.3 Phosphorene.

Black phosphorus (BP) is a layered semiconductor material with a *corrugated* hexagonal structure in each monolayer (phosphorene). As shown in fig.**3.4**, phosphorene has two main directions: *armchair* and *zigzag*. Such material comprises an orthorhombic tessellation of phosphorus atoms linked by covalent bonds, and each layer is bound by van der Waals forces.

Numerical and theoretical studies have revealed that when exposed to electromagnetic fields, dependency on polarization is observed within the properties of surface plasmons, and dependency on each monolayer's size, quantized magnetic field, among other phenomena [5]. All of this is due to its high anisotropy. For instance, the material has an anisotropic band structure and its charge carriers have anisotropic effective mass (as we will see later).

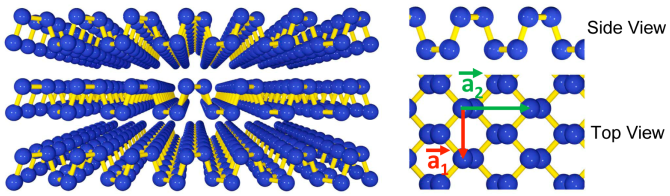

Figure **3.4**: Anisotropic structure of phosphorene in its two main directions. Image taken from [5].

Phosphorene exhibits anisotropic conductivity, meaning its electrical properties vary with crystallographic direction [9]. This anisotropy arises from the puckered structure of phosphorene and

the different electronic band structures along distinct crystallographic directions (fig. **3.5**). As mentioned above, the effective mass of charge carriers, such as electrons or holes, plays a crucial role in determining the conductivity of a material. It describes how the carriers respond to an applied electric field and is directly related to their mobility. For instance, along the armchair direction, phosphorene behaves as a semiconductor. The effective mass of charge carriers in this direction significantly influences the conductivity. For electrons, the effective mass determines their mobility and the ease with which they can contribute to electrical conduction. In phosphorene, the effective mass of electrons in the armchair direction is relatively small compared to the zigzag direction [10], leading to enhanced electron mobility and higher conductivity. In contrast, along the zigzag direction, phosphorene exhibits metallic behavior due to the overlap of electronic bands. The effective mass of charge carriers in the zigzag direction, particularly for electrons, affects the material's conductivity. The metallic behavior in this direction implies that the effective mass of electrons may be relatively larger compared to the armchair direction, but still allows for efficient electron transport and high conductivity due to the absence of a bandgap. Moreover, the effective mass of charge carriers in phosphorene may also exhibit temperature dependence, influencing its conductivity at different temperatures. Changes in temperature can alter the scattering mechanisms that affect carrier mobility, impacting the effective mass and overall conductivity of the material [7].

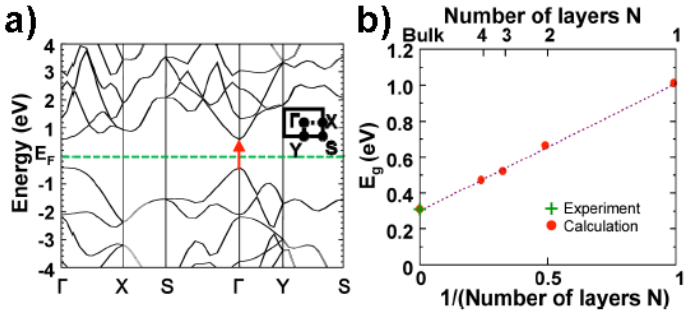

Figure **3.5**: a) Band structure of a phosphorene monolayer. b) Dependence of the energy gap in few-layer phosphorene on the number of layers. Picture taken from [5].

Understanding the effective mass of charge carriers in phosphorene is crucial for designing and optimizing electronic devices based on this material. By controlling the crystallographic orientation and thickness of phosphorene flakes, researchers can tailor its electronic properties and exploit its anisotropic conductivity for various applications, such as field-effect transistors, photodetectors, and thermoelectric devices. Finally, other interesting properties are its high mobility and highly tunable when exposed to an electromagnetic field, and its direct bandgap (0.3 eV in bulk to 2 eV in a monolayer) [7, 11].

1.4 Electric Field effect.

The electric field effect is a physical phenomenon that occurs when the electrical conductivity (current concentration) of a material is controlled or modulated by applying an external electric field to vary its electrical output as a semiconductor. It has been observed that in metals, there is a high concentration of electrons, for instance we have a high electron density. Due to this, when an electric field is applied to a metal, it can't penetrate deeply. However, semiconductors have fewer electrons available to respond to an applied electric field. Because of the lower electron density, the electric field can penetrate deeper into a semiconductor. The penetration of the electric field alters how conductive the semiconductor is, especially near its surface [12]. This phenomenon is crucial for the operation of certain electronic components like the Schottky diode and field-effect

transistors (MOSFET, JFET, MESFET) utilizing the field effect to control the flow of current, enabling functions like amplification and switching in electronic circuits.

1.4.1 Electric field effect in graphene.

One of the most intriguing aspects of graphene is its response to electric fields. First, recall that graphene's electronic structure is characterized by its linear energy dispersion near the Dirac points (see fig.**2.3**). This linear dispersion gives rise to massless Dirac fermions, behaving as relativistic particles with zero effective mass [13]. The Dirac point is special in graphene's electronic band structure, where the valence and conduction bands meet. It serves as the reference energy level for the Fermi energy. At the Dirac point, the Fermi level coincides with the energy of the Dirac point, resulting in a semimetallic behavior. Then, the electric field effect in graphene refers to the modulation of graphene's electronic properties by an external electric field perpendicular to its plane. This external field induces a potential difference across the graphene sheet, leading to changes in the carrier density and Fermi level position. By applying a gate voltage to a graphene device, one can control the carrier density in graphene [12]. When a positive gate voltage is applied, it attracts electrons towards the graphene surface, increasing the electron density and shifting the Fermi level upwards. Conversely, a negative gate voltage repels electrons, leading to a decrease in electron density and a downward shift of the Fermi level (see fig. **4.6**).

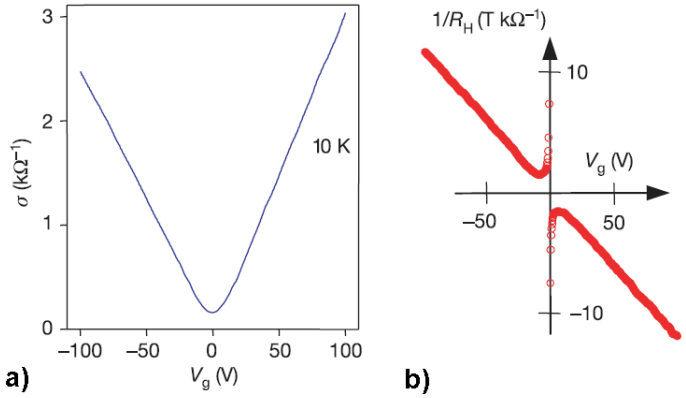

Figure **4.6**: a) Linear dispersion at the Dirac point for graphene's conductivity σ. b) Quantum Hall coefficient $1/R_H$. Both as a function of gate voltage V_g. Diagrams taken from [13].

Graphene exhibits ambipolar conduction, meaning it can support both electron and hole charge carriers. By adjusting the gate voltage, one can switch between electron and hole conduction regimes, making graphene highly versatile for electronic applications. In addition to carrier density modulation, the electric field effect in graphene also involves quantum capacitance effects. Due to graphene's two-dimensional nature and low density of states, it exhibits strong screening of external electric fields, resulting in a high quantum capacitance [14]. Can also modulate the optical properties of graphene. By changing the carrier density, one can tune the absorption and transmission spectra. Another case is using graphene stacks that can be reconfigured dynamically, often through self-biasing mechanisms, to control terahertz plasmonic responses [14]. Research has even been done focused on Tamm states, which are localized states at the interface of periodic structures, specifically in graphene-based metamaterials; these states are localized to regions much smaller than the wavelength of the electromagnetic radiation involved [15].

The electric field effect forms the basis for graphene field-effect transistors (GFETs), where the gate voltage controls the conductivity of the graphene channel. GFETs offer advantages such as high carrier mobility, low power consumption, and compatibility with flexible and transparent substrates, making them promising for next-generation electronics. Under strong magnetic fields

perpendicular to the graphene plane, the combination of the electric field effect and quantum confinement leads to the observation of the quantum Hall effect in graphene (see fig. **4.6**. (b)). Furthermore, graphene-based structures can exhibit topological insulating behavior under specific conditions, opening up possibilities for novel electronic and spintronic devices.

1.4.2 Electric field effect in phosphorene.

In case for phosphorene, as we saw in sec. (1.3), it has a direct bandgap, which is variable depending on the layer thickness. This makes it useful for applications in electronics and optoelectronics [5]. The electric field effect in phosphorene works similarly to how it does in other 2D materials but with some unique features due to its anisotropic nature. By applying an external electric field using a gate electrode, you can control the electronic properties of phosphorene. This is done by placing a gate electrode on or near the phosphorene layer, separated by an insulating layer (see fig. **4.7**). Because phosphorene is a 2D material, the electric field can penetrate effectively across its thickness. This allows the field to directly influence the electronic properties of the entire layer, unlike in bulk materials where the field might only affect a surface region. The electric field affects the distribution of charge carriers (electrons and holes) in phosphorene. Adjusting the gate voltage, can either increase or decrease the carrier concentration. This modulation changes the material's electrical conductivity. Typically, a positive gate voltage will attract electrons to the phosphorene layer, enhancing its n-type conductivity. Conversely, a negative gate voltage can attract holes (or repel electrons), increasing the p-type conductivity [4]. The electric field effect enables the use of phosphorene in field-effect transistors (FETs). This can lead to high-performance electronic devices with adjustable properties. Phosphorene-based transistors can potentially offer advantages like high carrier mobility and flexibility. Depending on their effective mass, the effective plasma frequency of phosphorene can be tuned by adjusting the carrier density. This is typically achieved using an external electric field through a gate electrode. By changing the gate voltage, it's possible modify the density of free electrons or holes in the phosphorene layer [16]. The ability to control the bandgap of phosphorene with an electric field is useful for optoelectronic applications, such as photodetectors and light-emitting devices. Adjusting the bandgap with an electric field allows for tunable optical properties. Research has even begun to focus combining of multiple 2D materials to achieve devices with particular structures, especially through vertical stacking, forming what are called van der Waals (vdW) heterostructures [17, 18, 19]. Due to its sensitivity to external fields, phosphorene can be used in sensors to detect changes in electric fields or other environmental parameters. This material can be sensitive to environmental conditions, such as moisture and oxygen, which may affect its performance and stability. Producing high-quality, uniform phosphorene layers and integrating them into devices at scale remains a technical challenge.

In summary, the electric field effect plays a crucial role in modulating the electronic and optical properties of graphene and phosphorene, enabling a wide range of applications in electronics, photonics, sensing, and quantum phenomena research. Its tunability and other remarkable characteristics continue to drive research and innovation in graphene/phosphorene-based technologies.

1.5 Conductivity.

The conductivity as the linear response of an electron to an electric field, describes how easily charge carriers (such as electrons) move in response to an applied electric field within a material. This concept is fundamental in condensed matter physics and plays a key role in understanding the electrical properties of materials. In the next section, we theoretically explore the interaction of the internal electric field in a photonic crystal, by analyzing the Kubo formalism and the Drude model in graphene and phosphorene.

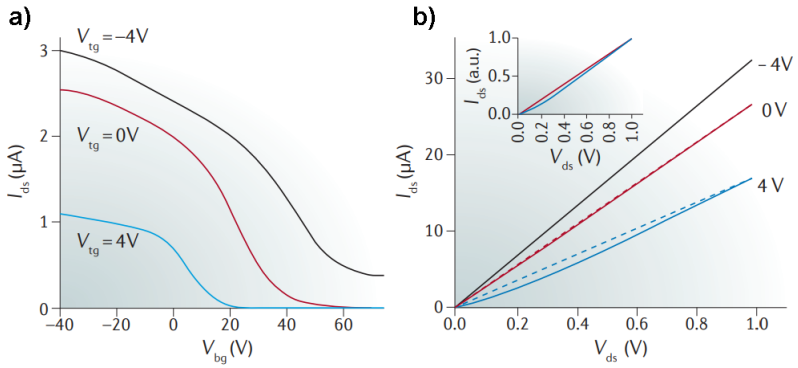

Figure **4.7**: a) Back-gate voltage (V_{bg}) dependence of the drain–source current (I_{ds}) at different top-gate voltage values (V_{tg}). b) Drain–source voltage (V_{ds}) dependence of the bias current at different displacement fields. Diagrams taken from [9].

1.5.1 Kubo's formula.

To describe a quantum system of many particles in principle, we have the Schrodinger equation:

$$i\frac{d}{dt}\left|\psi\left(t\right)\right\rangle = \hat{H}\left|\psi\left(t\right)\right\rangle. \tag{1.1}$$

This equation allows us to know the evolution of a quantum state in time from the Hamiltonian H. Pushing a system in thermal equilibrium; to out of equilibrium the *linear response theory appears*: Consider a quantum system described by the time-independent Hamiltonian $\hat{H}_0$. This system is assumed to be in thermal equilibrium (Gibbs state),

$$\rho = \frac{1}{Z}e^{-\beta\hat{H}_0} \tag{1.2}$$

as in ref. [20]. From the eigenvalue problem of the Hamiltonian

$$\hat{H}_0\left|E_k\right\rangle = E_k\left|E_k\right\rangle \tag{1.3}$$

we can expand the exponential in eq. (1.2) as the following expression:

$$e^{-\beta\hat{H}_0} = \sum_m e^{-E_m}\left|E_m\right\rangle\left\langle E_m\right| \tag{1.4}$$

and the partition function is written as the following formula

$$Z = \sum_m e^{-\beta E_m}. \tag{1.5}$$

Now, the expectation value of some observable A which in the thermal state is given as follows

$$\left\langle A\right\rangle_{\beta,0} = \frac{1}{Z}\sum_m e^{-\beta E_m}\left\langle E_m\right|A\left|E_m\right\rangle, \tag{1.6}$$

here, the two subscripts β and 0 indicate that is a thermal average with respect to the Hamiltonian and is taken at the thermodynamic beta, in this way, our state ρ and our observable A are time-independent. At $t \geq 0$ we will turn on a brand time dependent external perturbation, for instance the new Hamiltonian is

$$H\left(t\right) = H_0 + \lambda V\left(t\right), \tag{1.7}$$

we are going to treat H_0 as the free Hamiltonian and $\lambda V(t)$ as the interacting Hamiltonian. Now, we know that in the Schrodinger picture, the eigenstates of the H_0 evolve in time according to eq. (1.1), so this is

$$i\frac{\partial}{\partial t}|E_m(t)\rangle = H(t)|E_m(t)\rangle \tag{1.8}$$

and to re-express the time evolution in terms of the interaction picture is

$$|E_m(t)\rangle = e^{-iH_0t}|E_m(t)\rangle_{int} \tag{1.9}$$

where $|E_m(t)\rangle_{int}$ is the interaction picture state, defined as

$$|E_m(t)\rangle_{int} = U(t)|E_m(0)\rangle \tag{1.10}$$

which links t with the initial conditions, $U(t)$ is a time evolution operator that could be expanded by the Dyson series and only keep terms in the up until the first order; this gives us the following expression:

$$U(t) = 1 - i\lambda\int_0^t dt' V_{int}(t) \tag{1.11}$$

here,

$$V_{int}(t) = e^{iH_0t}V(t)e^{-H_0t}. \tag{1.12}$$

Re-writing eq. (1.6), we have

$$\langle A(t)\rangle = \frac{1}{Z}\sum_m e^{-\beta E_m}\langle E_m(t)|A|E_m(t)\rangle \tag{1.13}$$

and can insert the definitions from the interaction picture into expectation value, doing the following expression

$$\langle A(t)\rangle = \langle A\rangle_{\beta,0} - i\lambda\int_0^t dt'\frac{1}{Z}\sum_m e^{-\beta E_m}\langle E_m|\left[A_{int}(t)V_{int}(t') - V_{int}(t')A_{int}(t)\right]|E_m\rangle \tag{1.14}$$

simplifying and generalizing, we obtain the Kubo formula:

$$\langle\hat{A}(t)\rangle = \langle\hat{A}\rangle_0 - \frac{i}{\hbar}\int_{t_0}^t dt'\left\langle\left[\hat{A}(t),\hat{V}(t)\right]\right\rangle_0. \tag{1.15}$$

It was found that the transport mechanism must be related to diffusion on electrons [21]. Let us consider the case of a uniform system subjected to an external electric field $\vec{E}$, whose corresponding Hamiltonian is

$$H(t) = \frac{1}{2m}\sum_i\left[p_i + e\vec{A}(r_i,t)\right]^2 + U(r_i) \tag{1.16}$$

where m is the mass of the i-th electron, p the momentum, $\vec{A}$ is a vectorial potential and U is the potential energy function. Next, using relations, the eq. (1.16) can be rewritten as

$$H = \frac{i}{\omega}\int d\vec{r}\hat{J}(r)\cdot\vec{E}(r)e^{-i\omega t} \tag{1.17}$$

with the current density operator $\hat{J}(r)$ defined by

$$\hat{J}(r) = -\frac{e}{2m}\sum_i \left[\hat{p}_i \delta\left(\vec{r}-\vec{r}_i\right) - \delta\left(\vec{r}-\vec{r}_i\right)\hat{p}_i\right] \tag{1.18}$$

then, the conductivity σ can be defined as:

$$\sigma(\omega) = \frac{ine^2}{m\omega} + \frac{1}{\hbar\omega V}\int_0^\infty e^{i\omega t}\left\langle\left[\hat{J}(t), \hat{J}(0)\right]\right\rangle dt. \tag{1.19}$$

1.5.2 Graphene conductivity.

To describe the electronic properties of graphene, in the local limit $\omega \gg \tau^{-1}$, we can take eq. (1.19) for a given temperature T:

$$\sigma(\omega) = \frac{ie^2}{\pi\hbar}\left[\frac{\mu}{\hbar\left(\omega + i\tau^{-1}\right)} - \frac{1}{4}\ln\left(\frac{2\mu + \hbar\left(\omega + i\tau^{-1}\right)}{2\mu - \hbar\left(\omega + i\tau^{-1}\right)}\right)\right]. \tag{1.20}$$

The conductivity σ in these materials has two contributions: the intra-band and inter-band transitions. The first, in the classical Drude model approximation, is

$$\sigma_{intra}(\omega) \approx \frac{ie^2\mu}{\pi\hbar^2\left(\omega + i\tau^{-1}\right)} \tag{1.21}$$

and the second, is defined as follows

$$\sigma_{inter}(\omega) \approx -\frac{ie^2}{4\pi\hbar}\ln\left[\frac{2\mu + \hbar\left(\omega + i\tau^{-1}\right)}{2\mu - \hbar\left(\omega + i\tau^{-1}\right)}\right] \tag{1.22}$$

where e is the electron charge, μ is the Fermi level, $\hbar$ is the reduced Planck constant, and τ is the relaxation time [22, 23].

1.5.3 Phosphorene conductivity.

On the other hand, the conductivity of phosphorene (black phosphorus) is influenced by various factors, including its electronic band structure and the effective mass of charge carriers [10].

In summary, the effective mass of charge carriers in phosphorene significantly influences its conductivity, with smaller effective masses generally associated with higher conductivity. Understanding the anisotropic conductivity and effective mass of charge carriers in phosphorene is essential for leveraging its unique properties in electronic and optoelectronic applications.

The anisotropic conductivity of phosphorene can be described as:

$$\sigma_{jj}(\omega) = \frac{iD_j}{\pi\left(\omega + i\frac{\eta}{\hbar}\right)} \tag{1.23}$$

where j denotes the direction of propagation of the SP in the x (arm-chair) or y (zig-zag) direction. Then,

$$D_j = \frac{\pi e^2 N}{m_j} \tag{1.24}$$

is the Drude weight, which depends on the charge carrier density N and the anisotropic effective electron mass m_j, which are

$$m_x = \frac{\hbar^2}{\left(2\frac{\gamma^2}{\Delta} + \eta_c\right)} \tag{1.25}$$

$$m_y = \frac{\hbar^2}{2\nu_c} \tag{1.26}$$

where Δ, η_c, and ν_c are parameters of the conduction band. An important result is that: $m_x \approx 0.15 m_0$ and $m_y \approx 0.7 m_0$, with $m_0 = 0.51$ MeV is the invariant mass of an electron [11].

Chapter 2

Theoretical Model

In this chapter, we explain the theory of the processes followed to obtain the models and equations to be used. Starting from the TM polarization formalism at an interface of two different media. Then, we try to calculate the transmission and reflection amplitudes of a plane wave for such a polarization using the transfer matrix technique, which considers all the contributions of the incident plane wave in a very efficient way. Then, we try to calculate the transmission and reflection amplitudes of a plane wave for such a polarization using the transfer matrix technique, which takes into account all the contributions of the incident plane wave in a very efficient way. We first obtain a general expression for the transfer matrix of our experimental setup then we apply mathematical tools and special functions with the obtained formulas to achieve our specific objectives.

2.1 Plasmonics in 2D Materials.

Plasmonics refers to the interaction of incident electromagnetic waves with the free electrons of a metal [24]. When light interacts with a metal surface, it can excite collective oscillations of electrons, known as surface plasmons (SPs). The electromagnetic fields associated with SPs guided by highly conductive metallic surfaces at mid-infrared (MIR) and Terahertz (THz) frequencies are similar to plane waves that propagate ubiquitously at the interface of the dielectric medium. 2D materials present several advantages in plasmonics due to their electronic and optical properties. Some materials mentioned in Chapter 1.1, for example, exhibit high carrier mobility, broad spectral response, and plasmonic properties tunable by gate voltage modulation. Others possess considerable bandgap and strong light-matter interactions, allowing efficient control of plasmonic modes. Consider also that there are those that provide excellent dielectric properties, which facilitates strong plasmonic coupling.

The dispersion relation can be derived from Maxwell's equations with appropriate approximations and boundary conditions. Remember that, Maxwell's equations in the absence of external charge and current density are [25]:

$$\boldsymbol{\nabla} \cdot \vec{D} = 0 \tag{2.1}$$

$$\boldsymbol{\nabla} \cdot \vec{B} = 0 \tag{2.2}$$

$$\boldsymbol{\nabla} \times \vec{E} = -\frac{1}{c}\frac{\partial \vec{B}}{\partial t} \tag{2.3}$$

$$\boldsymbol{\nabla} \times \vec{H} = \frac{1}{c}\frac{\partial \vec{D}}{\partial t} \tag{2.4}$$

where $\vec{D}$ is the dielectric displacement, $\vec{B}$ the magnetic induction, $\vec{E}$ the electric field and $\vec{H}$ the magnetic field. If $\vec{D} = \epsilon\vec{E}$ y $\vec{H} = \vec{B}/\mu$, we rewrite eq. (2.4), such that

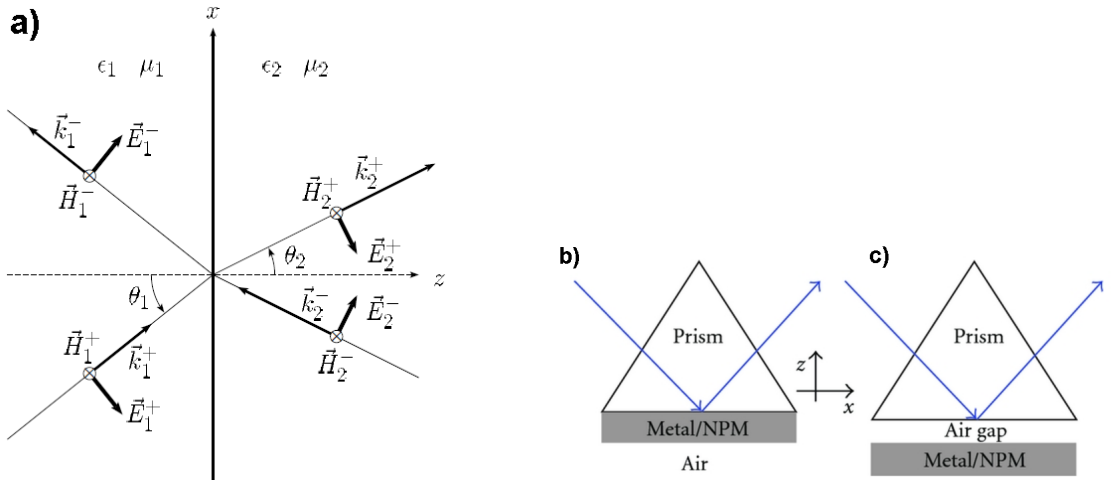

Figure **1.1**: a) Frame for TM polarization. b) Kretschmann configuration. c) Otto configuration.

$$\boldsymbol{\nabla} \times \vec{B} - \frac{\epsilon\mu}{c}\frac{\partial \vec{E}}{\partial t} = 0. \tag{2.5}$$

Now, applying rotational to eq. (2.3) we have

$$\begin{aligned} \boldsymbol{\nabla} \times \left(\boldsymbol{\nabla} \times \vec{E} + \frac{1}{c}\frac{\partial \vec{B}}{\partial t} \right) &= 0 \\ \boldsymbol{\nabla} \times \left(\boldsymbol{\nabla} \times \vec{E} \right) + \frac{1}{c}\frac{\partial}{\partial t}\left(\boldsymbol{\nabla} \times \vec{B} \right) &= 0 \\ \boldsymbol{\nabla} \left(\boldsymbol{\nabla} \cdot \vec{E} \right) - \nabla^2 \vec{E} + \frac{1}{c}\frac{\partial}{\partial t}\left(\boldsymbol{\nabla} \times \vec{B} \right) &= 0. \end{aligned} \tag{2.6}$$

Substituting eq. (2.5) in eq. (2.6) and, applying eq. (2.1), it is obtained that

$$\begin{aligned} -\nabla^2 \vec{E} + \frac{1}{c}\frac{\partial}{\partial t}\left(\frac{\epsilon\mu}{c}\frac{\partial \vec{E}}{\partial t} \right) &= 0 \\ \nabla^2 \vec{E} - \frac{\epsilon\mu}{c^2}\frac{\partial^2 \vec{E}}{\partial t^2} &= 0 \end{aligned} \tag{2.7}$$

whose solutions are of the type:

$$\vec{E}\left(\vec{r}, t\right) = \vec{E}_0 e^{i\left(\vec{k}\cdot\vec{r} - \omega t\right)}. \tag{2.8}$$

Then, considering electromagnetic waves propagating as a planar wavefront at the interface between two media 1 and 2 (see fig. **1.1**. a), there is a component of the electric field perpendicular to the interface (considering TM polarization) that contributes to the formation of an SP. Now, being $\vec{r} = x\hat{x} + y\hat{y} + z\hat{z}$, $\vec{E} = E_x\hat{x} - E_z\hat{z}$ and the wave vector $\vec{k} = k_x\hat{x} + k_z\hat{z}$, we have

$$\vec{k} \cdot \vec{r} = k_x x + k_z z \tag{2.9}$$

$$\vec{k} \times \vec{E} = \left[\left(k_x E_z + k_z E x \right) e^{i\left(k_x x + k_z z - \omega t\right)} \right] \hat{y} \tag{2.10}$$

from last expression, let us note that if $\vec{k} \times \vec{E} = \omega/c\vec{B}$, being ω the angular frequency, it can be deduced that

$$k_x E_z + k_z Ex = \frac{\omega}{c} B_y. \tag{2.11}$$

On the other hand, from eq. (2.1) it follows that

$$\begin{aligned} \boldsymbol{\nabla} \cdot \epsilon \vec{E} &= 0 \\ ik_x E_x e^{i(k_x x + k_z z - \omega t)} - ik_z E_z e^{i(k_x x + k_z z - \omega t)} &= 0 \end{aligned} \tag{2.12}$$

clearing from eq. (2.12)

$$\Rightarrow E_z = \frac{k_x}{k_z} E_x. \tag{2.13}$$

Thus, substituting (2.13) in (2.11) and, remembering that the wavenumber $k^2 = \omega^2 \epsilon \mu / c^2$, we have that

$$\begin{aligned} \frac{\omega}{c} B_y &= k_x \left(\frac{k_x}{k_z} E_x \right) + k_z Ex \\ &= \left(\frac{{k_x}^2}{k_z} + k_z \right) E_x \\ &= \frac{k^2}{k_z} E_x \\ &= \left(\frac{\omega^2 \epsilon \mu}{c^2 k_z} \right) E_x. \end{aligned} \tag{2.14}$$

Solving for eq. (2.14) it seems that:

$$\frac{H_{y_i}}{E_{x_i}} = \frac{\omega \epsilon_0 \epsilon_i}{c k_{z_i}} \equiv \mathbb{Z}_i \tag{2.15}$$

defining $\mathbb{Z}$ as impedance, where i denotes media 1 and 2, respectively. Now, to extract information from Eqs. (2.15), boundary conditions for the electromagnetic field are required, which can be derived from the integral forms of equations (2.3) and (2.4):

$$\oint \vec{E} \cdot d\vec{l} = -\frac{1}{c} \frac{d}{dt} \iint \vec{H} \cdot d\vec{s} \tag{2.16}$$

$$\oint \vec{H} \cdot d\vec{l} = \frac{\epsilon}{c} \frac{d}{dt} \iint \vec{E} \cdot d\vec{s} \tag{2.17}$$

After integrating Eqs. (2.16) and (2.17) around an infinitesimally thin circuit containing the interface and a thin layer with surface conductivity σ proportional to a conducting current $\vec{J} = \sigma \vec{E}$, the boundary conditions are:

$$Ex_1 = E_{x_2} \tag{2.18}$$

$$H_{y_2} - H_{y_1} = J_{x_1} \tag{2.19}$$

where $J_{x_1} = \sigma E_{x_1}$; but they can also be expressed with the help of (2.15) in the following system of equations

$$E_{x_1} - E_{x_2} = 0 \tag{2.20}$$

$$(\mathbb{Z}_1 + \sigma)\, E_{x_1} + \mathbb{Z}_2 E_{x_2} = 0 \tag{2.21}$$

or also in matrix form

$$\begin{pmatrix} 1 & -1 \\ \mathbb{Z}_1 + \sigma & \mathbb{Z}_2 \end{pmatrix} \begin{pmatrix} E_{x_1} \\ E_{x_2} \end{pmatrix} = \begin{pmatrix} 0 \\ 0 \end{pmatrix} \tag{2.22}$$

which has a non-trivial solution if and only if the determinant of the square matrix is null, this is

$$\mathbb{Z}_1 + \mathbb{Z}_2 + \sigma = 0 \tag{2.23}$$

Subsequently:

$$\frac{{n_1}^2}{k_{z_1}} + \frac{{n_2}^2}{k_{z_2}} + \frac{\sigma}{\omega\epsilon_0} = 0 \tag{2.24}$$

where $n_i = \sqrt{\epsilon_i \mu_i}$ corresponds to the refractive index of each medium.

2.2 Transfer Matrix.

Figure **2.2**: One-dimensional photonic crystal with a conducting two-dimensional material.

According to Figure (**2.2**), the fields in each medium are of the form

$$\begin{pmatrix} E_x \\ H_y \end{pmatrix} = \begin{pmatrix} E^+ + E^- \\ \frac{1}{\mathbb{Z}} E^+ - \frac{1}{\mathbb{Z}} E^- \end{pmatrix} \tag{2.25}$$

such that at z_0, the components of the electric field can be expressed as follows

$$E^-_{z_0} = Ae^{-ik_z z_0} = e^{-ik_z(z_0 - z)} Ae^{-ik_z z} = e^{-ik_z(z_0 - z)} E^-_z \tag{2.26}$$

$$E^+_{z_0} = Be^{ik_z z_0} = e^{ik_z(z_0 - z)} Be^{ik_z z} = e^{ik_z(z_0 - z)} E^+_z \tag{2.27}$$

such that, if we define $d = |z_1 - z_0|$, at z_1 the field components are

$$\begin{pmatrix} E^- \\ E^+ \end{pmatrix}_{z_1} = \begin{pmatrix} e^{-ik_z d} & 0 \\ 0 & e^{ik_z d} \end{pmatrix} \begin{pmatrix} E^- \\ E^+ \end{pmatrix}_{z_0}. \tag{2.28}$$

Let $\mathbb{Y}$ be the impedance matrix

$$\mathbb{Y}_j = \begin{pmatrix} 1 & 1 \\ -\frac{1}{\mathbb{Z}} & \frac{1}{\mathbb{Z}} \end{pmatrix}_j \tag{2.29}$$

such that equation (2.25) becomes

$$\begin{pmatrix} E_x \\ H_y \end{pmatrix}_z = \mathbb{Y}_j \begin{pmatrix} E^- \\ E^+ \end{pmatrix}_z \tag{2.30}$$

$$\Rightarrow \begin{pmatrix} E_x \\ H_y \end{pmatrix}_{z_1} = \mathbb{Y}_1 \begin{pmatrix} E^- \\ E^+ \end{pmatrix}_{z_1} {\mathbb{Y}_1}^{-1} \begin{pmatrix} E_x \\ H_y \end{pmatrix}_{z_0} = \mathbb{P}_1 \begin{pmatrix} E_x \\ H_y \end{pmatrix}_{z_0}, \tag{2.31}$$

where $\mathbb{P}$ is defined as the matrix

$$\mathbb{P}_j = \mathbb{Y}_j \begin{pmatrix} E^- \\ E^+ \end{pmatrix}_{z_j} {\mathbb{Y}_j}^{-1}. \tag{2.32}$$

Now, solving for ${z_1}'$ with boundary conditions:

$$\begin{pmatrix} E_x \\ H_y \end{pmatrix}_{{z_1}'} = \begin{pmatrix} 1 & 0 \\ -\sigma & 1 \end{pmatrix} \begin{pmatrix} E_x \\ H_y \end{pmatrix}_{z_1} \tag{2.33}$$

we can define $\mathbf{M}$ as the unit cell transfer matrix, this is

$$\mathbf{M} = \begin{pmatrix} 1 & 0 \\ -\sigma & 1 \end{pmatrix} \mathbb{P}_j \tag{2.34}$$

then, by (2.31) and (2.34), equation (2.36) becomes:

$$\begin{pmatrix} E_x \\ H_y \end{pmatrix}_{{z_1}'} = \mathbf{M} \begin{pmatrix} E_x \\ H_y \end{pmatrix}_{z_0}. \tag{2.35}$$

For a periodic array of N layers and with (2.30), the previous expression can be formulated as follows:

$$\begin{pmatrix} 0 \\ E^+ \end{pmatrix}_{{z_1}'} = \begin{pmatrix} m_{11} & m_{12} \\ m_{21} & m_{22} \end{pmatrix}^N \begin{pmatrix} E^- \\ 0 \end{pmatrix}_{z_0} \tag{2.36}$$

where

$$m_{11} \equiv A = e^{-ik_z d} \left(1 + \frac{\mathbb{Z}_2}{\mathbb{Z}_1} + \sigma \mathbb{Z}_2 \right) \tag{2.37}$$

$$m_{12} \equiv B = e^{ik_z d} \left(1 - \frac{\mathbb{Z}_2}{\mathbb{Z}_1} + \sigma \mathbb{Z}_2 \right) \tag{2.38}$$

$$m_{21} \equiv C = e^{-ik_z d} \left(1 - \frac{\mathbb{Z}_2}{\mathbb{Z}_1} - \sigma \mathbb{Z}_2 \right) - \sigma e^{-ik_z d} \left(1 + \frac{\mathbb{Z}_2}{\mathbb{Z}_1} + \sigma \mathbb{Z}_2 \right) \tag{2.39}$$

$$m_{22} \equiv D = e^{ik_z d} \left(1 + \frac{\mathbb{Z}_2}{\mathbb{Z}_1} - \sigma \mathbb{Z}_2 \right) - \sigma e^{ik_z d} \left(1 - \frac{\mathbb{Z}_2}{\mathbb{Z}_1} + \sigma \mathbb{Z}_2 \right) \tag{2.40}$$

2.3 Chebyshev Polynomials.

For confined modes, the condition is that $A = 0$ [26]. Then, using the Chebyshev second-kind trigonometric identity:

$$U_n (\cos\theta) = \frac{\sin (n+1)\,\theta}{\sin\theta} \tag{2.41}$$

where $n \in \mathbf{N}$; the dispersion modes relationship for a system of N layers is given by

$$A \frac{\sin NK\Lambda}{\sin K\Lambda} - \frac{\sin (N-1)\,K\Lambda}{\sin K\Lambda} = 0 \tag{2.42}$$

with

$$K\Lambda = \arccos \frac{1}{2}(A + D) \tag{2.43}$$

2.4 Dispersion Relations.

With the eq. (2.42) we can plot the dispersion relations for a several periodic systems with a different number of layer N. Figure (**4.3**) shows the contour plot for a one-dimensional photonic crystal with different number of graphene layers, ranging from $N = 1$ layer to $N = 15$ layers.

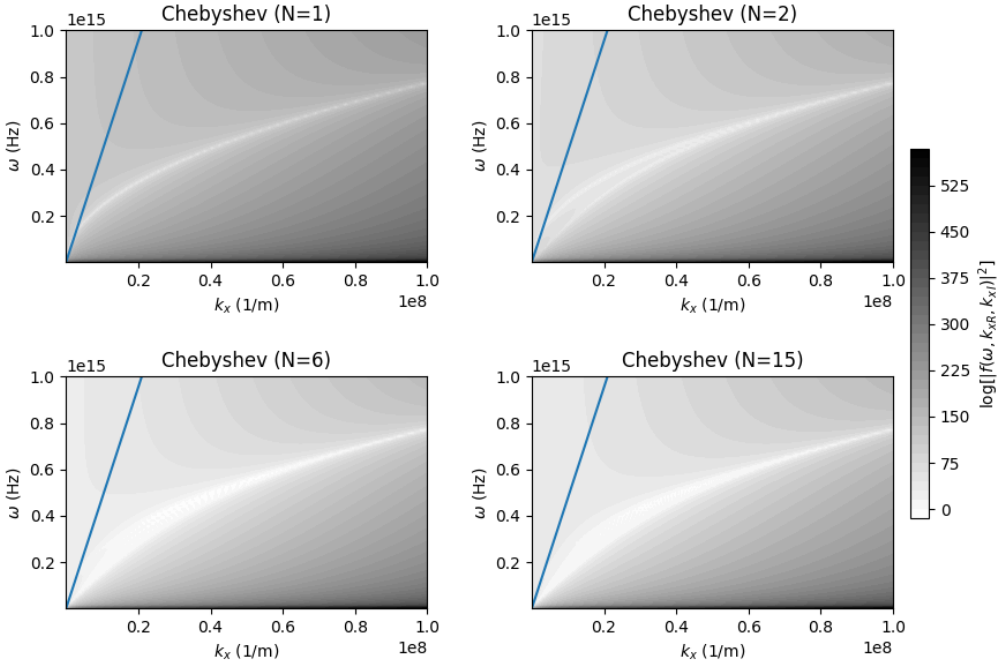

Figure **4.3**: Dispersion relations for different number of graphene layers with $n_1 = n_2 = 1.6$, $\mu = 0.9eV$, $\tau = 1ps$ using the Chebyshev relation (2.42). Blue line is the light line.

Note that for a region of very small k_x values and below the light line, there seems to be a splitting of these modes, but beyond a certain critical value these modes tend to be suppressed in the four cases presented.

2.5 Bloch's theorem.

It is necessary to consider an important result in order to know the solutions of the Schrodinger equation in a periodic potential. Bloch's theorem is a fundamental result in solid-state physics that describes the behavior of electrons in a periodic potential, such as the potential inside a crystalline solid. It is named after the Swiss physicist F. Bloch, who formulated it in 1929 [27].

We have that in a crystal, the potential energy experienced by an electron is periodic with the same periodicity as the crystal lattice. Bloch's theorem states that the wave-functions of electrons in such a periodic potential can be expressed as a product of a plane wave and a function with the same periodicity as the lattice [28]. Mathematically, this is written as:

$$\psi_{\vec{k}}(\vec{r}) = u_{\vec{k}}(\vec{r})\, e^{i\vec{k}\cdot\vec{r}} \tag{2.44}$$

where:

- $\psi_{\vec{k}}(\vec{r})$ is the eigenfunction of the wave equation.
- $\vec{k}$ is the wavevector related to the momentum of an electron, which is confined to the first Brillouin zone.
- $u_{\vec{k}}(\vec{r})$ is a function that has the same period as the crystal lattice with $u_{\vec{k}}(\vec{r}) = u_{\vec{k}}\left(\vec{r}+\vec{T}\right)$. Here $\vec{T}$ is a translation vector of the lattice.
- $e^{i\vec{k}\cdot\vec{r}}$ is the plane-wave term.

In solid-state physics, electrons in a crystal lattice experience a periodic potential due to the regular arrangement of atoms. This periodicity affects the electronic properties of the material, leading to the formation of energy bands rather than discrete energy levels. Recall that the time-independent Schrödinger equation for an electron in a crystal is given by eq. (1.8), which we can also express as follows:

$$\left[-\frac{\hbar^2}{2m}\nabla^2 + V(\vec{r})\right]\psi_k(\vec{r}) = E_k\psi_k(\vec{r}) \tag{2.45}$$

where:

- $\hbar$ is the reduced Planck constant.
- m is the electron mass.
- $V(\vec{r})$ is the periodic potential due to the crystal lattice.
- E_k is the energy of the electron,

according to ref.[29]. Substituting eq. (2.44) into eq. (2.45) yields:

$$\left[-\frac{\hbar^2}{2m}\left(\nabla^2 - 2i\vec{k}\cdot\nabla + \vec{k}^2\right) + V(\vec{r})\right]e^{i\vec{k}\cdot\vec{r}}u_k(\vec{r}) = E_k e^{i\vec{k}\cdot\vec{r}}u_k(\vec{r}) \tag{2.46}$$

$$\left[-\frac{\hbar^2}{2m}\left(\nabla^2 - 2i\vec{k}\cdot\nabla + \vec{k}^2\right) + V(\vec{r})\right]u_k(\vec{r}) = E_k u_k(\vec{r}) \tag{2.47}$$

Then, the Hamiltonian operator for the system is:

$$\hat{H} = -\frac{\hbar^2}{2m}\nabla^2 + V(\vec{r}) \tag{2.48}$$

Due to the periodicity of $V(\vec{r})$, we can express $V(\vec{r})$ as a Fourier series:

$$V(\vec{r}) = \sum_{\vec{G}} V_{\vec{G}} e^{i\vec{G}\cdot\vec{r}} \tag{2.49}$$

where $\vec{G}$ are the reciprocal lattice vectors. Consider the Hamiltonian in the basis of plane waves $e^{i\vec{k}\cdot\vec{r}}$. The Hamiltonian matrix elements between these plane waves are:

$$H_{\vec{k},\vec{k}'} = \langle e^{i\vec{k}\cdot\vec{r}}|\hat{H}|e^{i\vec{k}'\cdot\vec{r}}\rangle \tag{2.50}$$

The periodic potential $V(\vec{r})$ leads to matrix elements that couple different $\vec{k}$ states. The resulting matrix elements can be written as:

$$H_{\vec{k},\vec{k}'} = \left(-\frac{\hbar^2}{2m}(\vec{k}^2 + \vec{k}'^2) + \langle e^{i\vec{k}\cdot\vec{r}}|V(\vec{r})|e^{i\vec{k}'\cdot\vec{r}}\rangle \right). \tag{2.51}$$

To find the allowed energy levels, we solve the eigenvalue problem:

$$\hat{H}\psi_k(\vec{r}) = E_k\psi_k(\vec{r}) \tag{2.52}$$

Substituting $\psi_k(\vec{r}) = e^{i\vec{k}\cdot\vec{r}}u_k(\vec{r})$ and using the Fourier expansion of the potential, we obtain a set of coupled differential equations for $u_k(\vec{r})$. These equations must be solved to find the eigenvalues E_k as a function of $\vec{k}$. The solutions to the eigenvalue problem yield discrete energy levels E_k for each $\vec{k}$ in the Brillouin zone. These energies form continuous bands as $\vec{k}$ varies within the Brillouin zone, which are the **Allowed Bands**: Regions where the energy E_k is allowed for electrons; and the **Band Gaps**: Energy ranges between these bands where no electron states are available. The band structure of a solid is a plot of E_k as a function of $\vec{k}$. It reveals the allowed and forbidden energy levels for electrons [28, 29], either valence bands (typically filled with electrons) or conduction bands (can be empty or partially filled, allowing for conduction). And thus, it gives rise to the following classification: **Conductors**: Materials with overlapping valence and conduction bands or no band gap. **Semiconductors**: Materials with a small band gap between valence and conduction bands. **Insulators**: Materials with a large band gap that prevents electron flow.

Now, to determine the band structure in our 1D photonic crystal, by Bloch's theorem, we have that

$$\mathbf{M}\begin{pmatrix} E_x \\ H_y \end{pmatrix}_{z_0} = \mathbb{I}_{2x2}e^{iK_Bd}\begin{pmatrix} E_x \\ H_y \end{pmatrix}_{z_0} \tag{2.53}$$

factoring and rearranging, we find that (2.53) is possible if and only if

$$\left|\mathbf{M} - \mathbb{I}_{2x2}e^{iK_Bd}\right| = 0 \tag{2.54}$$

which leads us to

$$e^{-iK_Bd} + e^{iK_Bd} - (A + D) = 0, \tag{2.55}$$

or equivalently,

$$K_Bd = \arccos\left(\frac{1}{2}\,\mathrm{Tr}\{M\}\right). \tag{2.56}$$

2.6 Plasmonic bands.

The plasmonic band or surface plasmon band (SPB) is a phenomenon observed in some materials (such as gold or silver). It refers to the range of frequency over those materials exhibit strong interaction with electromagnetic waves due to surface plasmon resonances [30]. This leads to enhanced electromagnetic fields at the material's surface. Now, where electrons have allowed and forbidden energy ranges, some materials have specific ranges of frequencies where these surface plasmon resonances occur. These frequency ranges are known as plasmonic bands.

In our case, for graphene, the surface plasmons arise from the collective oscillations of the electrons in the material. Unlike conventional metals, graphene's plasmons are tunable due to its electronic structure and the ability to modify its chemical environment [31, 32]. More specifically, this response in graphene can be tuned across a broad range of frequencies, from terahertz to visible light, by adjusting external factors like the Fermi level and the gating voltage. This tunability results from graphene's linear energy-momentum relationship near the Dirac points. Fig. (**6.4**) shows the resulting plasmon dispersion in multilayer graphene for in-plane momentum transfers q along the ΓM direction which was considered in ref. [33], where aims to deepen the understanding

of plasmonic behavior in multilayer graphene by using advanced spectroscopy techniques, analyzing the high-energy plasmon modes and exploring the transition between 2D and 3D plasmon behaviors. On the other hand, for phosphorene, we have in a similar way the plasmonic behavior due to its anisotropic nature. This means that the plasmonic bands in phosphorene can be quite different in terms of frequency range and response compared to other materials. The frequency and behavior of plasmons in phosphorene can be controlled by factors like the material's thickness and the applied electric field [34]. Remembering that phosphorene has an anisotropic electronic structure, its electrical and optical properties vary with direction. This anisotropy can lead to unique plasmonic behaviors, such as directional dependence of plasmonic resonances and enhanced interaction with radiation in specific directions.

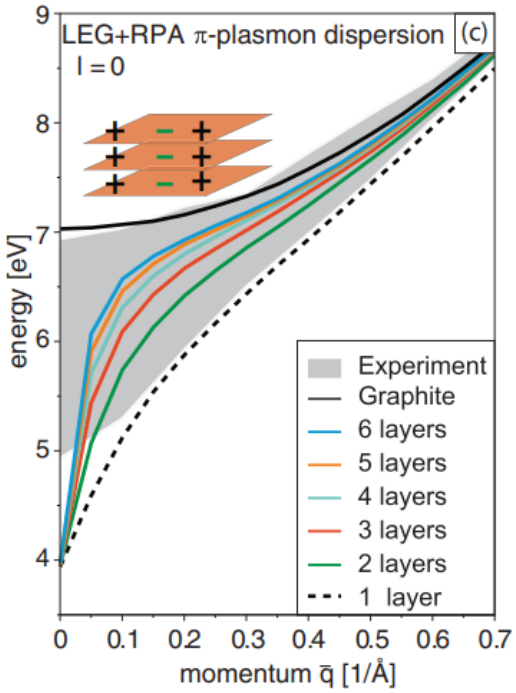

Figure **6.4**: Dispersion of the highest-energy plasmon band in multilayer graphene from two to six layers calculated using the RPA polarizability of graphene. Image extracted from [33].

In other words, the plasmonic bands lie in the terahertz to mid-infrared range. This range corresponds to the frequencies at which collective electron oscillations can be excited in graphene. The plasmonic behavior of graphene is primarily governed by its unique electronic structure, with linear energy dispersion near the Fermi level. The plasmonic response in graphene can be tuned over a wide spectral range by varying the Fermi energy through gate voltage or chemical doping. While phosphorene is primarily known for its semiconducting characteristics, it also supports plasmonic modes that can be harnessed for various applications. Phosphorene possesses multiple valleys in its electronic band structure, associated with distinct momentum states of charge carriers. These valleys can interact differently with external electromagnetic fields, leading to valley-selective plasmon excitation. This phenomenon enables selective manipulation of plasmonic modes in phosphorene based on the valley index, offering additional degrees of freedom for controlling light-matter interactions.

In a previous work [35], the characteristics of TM projected band structures and SPs in a 1D GPC (one-dimensional graphene-dielectric photonic crystal) were studied (see fig.**6.5**). It was found that pure SPs in the 1D GPC exhibit higher localization (they are more confined to the surface) and longer propagation lengths compared to SPs in a 1D metallic photonic crystal. This means they can

be more effectively used in devices requiring long-range interaction. Using graphene disks, extends the frequency range over which SPs are supported and results in wider bandgaps, which improves the far-infrared (far-IR) filtering capabilities of the photonic crystal. While using graphene sheets, is possible reducing the width of the dielectric layers causes the graphene absorption bandgaps to widen, broadens the frequency range of supported SPs also enhances the localization of pure SPs and increases their propagation length. Another work [36], demonstrates that the photonic response of a periodic stack of graphene monolayers can be significantly enriched by introducing sequential doping modulations. These modulations can be periodic, quasi-periodic, or harmonic, leading to varied and potentially complex photonic band structures. The fixed separation between layers creates a structural band gap, which can be adjusted by changing the doping levels through gating. Additionally, specific modulation profiles, like continuous cosine or semi-continuous square functions, give rise to frequency mini-bands within the photonic band structure. Another interesting topic in the field of nanophotonics and materials science is that in the presence of a suitable dielectric environment, graphene supports surface plasmons that can couple with the substrate's phonon-polariton modes. This coupling leads to hybrid modes where the characteristics of both surface plasmons and phonon-polaritons are present [37].

In a similar way to graphene, it is to be expected that the same is true for phosphorene: periodic structures can be introduced with this material to create a photonic band gap. The photonic band gap is achieved by designing periodic arrays or heterostructures that modify the local optical density of states and create regions where light propagation is forbidden.

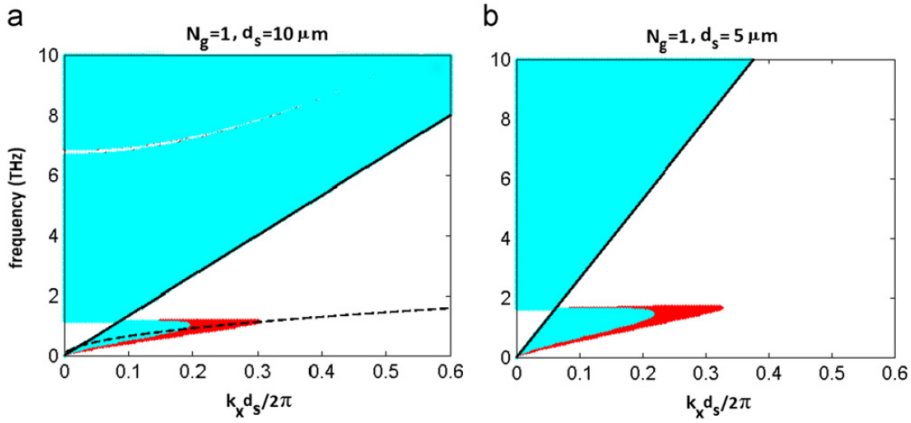

Figure **6.5**: TM projected band structure for different values of the distance between graphene sheets d_s. The shaded areas (red and aqua) correspond to the Bloch pass bands (lying above the light line) and the Bloch's evanescent band (lying below the light-line). The white areas correspond to the gaps. Also, the straight black lines show the light-line of the medium with a dielectric constant, and the black dashed curve in (a) shows the dispersion of SPs supported by a graphene sheet placed in $z = 0$ and surrounded with dielectric materials of constant known. Image extracted from [35].

Chapter 3

Results and discussions.

In this chapter, we analyze the results followed from Chapter 2 to observe how phosphorene and graphene-based materials exhibit distinct plasmonic responses. By examining the interplay between material properties, geometric configurations, and external stimuli, we aim to uncover the underlying principles governing plasmonic behavior in these systems, such as their propagation length, decay length and projected bands structures. We also give the main numerical results aiming to analyze the objectives of this work.

3.1 Plasmonic modes in graphene.

One important concept is to remember is that in 2D materials, plasmonic modes can be classified into two types: surface plasmon polaritons (SPP) and localized surface plasmons (LSP). SPPs are collective excitations that propagate along the interface of a 2D material and a dielectric, offering sub-wavelength confinement and large propagation lengths. LSPs, on the other hand, are confined to nanoscale regions, such as defects or edges of 2D materials, resulting in strong field localization and enhanced light-matter interactions [24]. Then, we begin the analysis of plasmonic modes by plotting graphene conductivity for different doping levels μ. In fig. (**1.1**), we can observe the behavior of conductivity for inter-band and intra-band transitions (according to eq. 1.20).

The conductivity is expressed in units of $\sigma' = e^2/4\hbar$ which is a dimensionless quantity and the real and imaginary parts of conductivities for each μ are plotted in different colors. At low frequencies, the real part of the conductivity is high for smaller μ, indicating that graphene is more conductive and the imaginary part is close to zero. As frequency increases, the real part decreases and stabilizes, while the imaginary part shows peaks that suggest a shift from conductive to capacitive behavior. So we can say that the doping level shifts the overall behavior of the conductivity. Higher μ leads to a more pronounced flat region in the real part and a sharper peak in the imaginary part, reflecting that the transition frequencies are shifted to higher frequencies. This implies that, at low THz frequencies, the leading conductivity comes from the intraband contribution.

Now, if we replace (1.21) into (2.24), we obtain the dispersion relation for a SPP in a graphene monolayer:

$$\frac{{n_1}^2}{k_{z_1}} + \frac{{n_2}^2}{k_{z_2}} + \frac{ie^2\mu}{\omega\epsilon_0\pi\hbar^2\left(\omega + i\tau^{-1}\right)} = 0. \tag{3.1}$$

Some approximations and numerical solutions to the equation (3.1) are presented below, citing the previous work [22]. Let us consider an incident wave-number,

$${k_j}^2 = {k_{SP}}^2 + {k_{z_j}}^2 \tag{3.2}$$

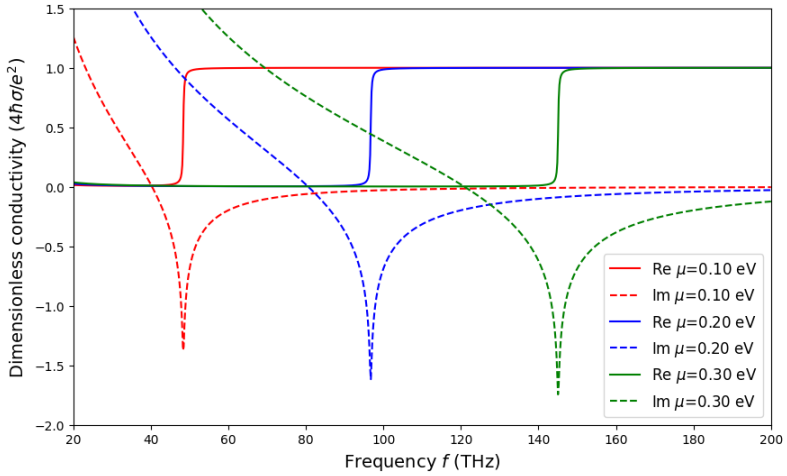

Figure **1.1**: Real and imaginary parts of conductivity expressed in units of $\sigma/\left(e^2/4\hbar\right)$, which is a dimensionless quantity, for $\mu = 0.1, 0.2, 0.3\ eV$ as a function of frequency, ranging from 0 to 2×10^{14} Hz. As the doping level increases, the transition frequencies ares shifted to higher frequencies.

where ${k_{SP}}^2$ corresponds to the component in the x direction and $j = 1, 2$ indicates mediums. Solving (3.2) for k_{z_j}, we have that

$$\begin{aligned} k_{z_j} =& \sqrt{{k_j}^2 - {k_{SP}}^2} \\ =& \sqrt{-(ik_j)^2 + (ik_{SP})^2} \\ =& i\sqrt{{k_{SP}}^2 - {k_j}^2} \end{aligned} \tag{3.3}$$

then, considering that $|k_{SP}|^2 \gg {k_j}^2$, the approximation is as follows

$$k_{z_j} = i\sqrt{{k_{sp}}^2 - {k_j}^2} \approx ik_{SP} \tag{3.4}$$

and hence $k_{z_1} = k_{z_2}$. Substituting this into eq. (2.24), we get that

$$\frac{{n_1}^2}{ik_{sp}} + \frac{{n_2}^2}{ik_{sp}} + \frac{ie^2\mu}{\omega\epsilon_0\pi\hbar^2\left(\omega + i\tau^{-1}\right)} = 0 \tag{3.5}$$

$$\therefore k_{sp} \approx \frac{\pi\epsilon_0\hbar^2\left({n_1}^2 + {n_2}^2\right)\left(\omega^2 + i\omega\tau^{-1}\right)}{\mu e^2}. \tag{3.6}$$

Now, from eq. (3.1) we have that

$$\frac{{n_1}^2}{\sqrt{{k_1}^2 - {k_x}^2}} + \frac{{n_2}^2}{\sqrt{{k_2}^2 - {k_x}^2}} + \frac{ie^2\mu}{\omega\epsilon_0\pi\hbar^2\left(\omega + i\tau^{-1}\right)} = 0 \tag{3.7}$$

where $k_j = k_0\sqrt{\epsilon_j}$, with $k_0 = \omega/c$ and $k_x = k_{x\,Re} + ik_{x\,Im}$ being a complex number. Reducing the above expression, we arrive at the following dispersion relation:

$$\frac{{n_1}^2}{\sqrt{\left(\frac{\omega}{c}\right)^2\epsilon_1 - \left(k_{xR} + ik_{xI}\right)^2}} + \frac{{n_2}^2}{\sqrt{\left(\frac{\omega}{c}\right)^2\epsilon_2 - \left(k_{xR} + ik_{xI}\right)^2}} + \frac{ie^2\mu}{\omega\epsilon_0\pi\hbar^2\left(\omega + i\tau^{-1}\right)} = 0; \tag{3.8}$$

which, we can define as a function f of three variables

$$f\left(\omega, k_{xR}, k_{xI}\right) = 0 \tag{3.9}$$

and its level surfaces can be plotted using the $\log|f|^2$ technique with a contour plot. In figure (**1.2**), we display the dispersion relation by this contour plot technique (an example code is shown in List. (A.1) of Appendix). The brighter regions correspond to higher intensities of the contour plot, i. e., in this region the eq. (3.9) is satisfied and shows where the SPPs are most strongly excited, according to the color-bar scale. Green dashed line shows the approximation taken in [22] with a Fermi level $\mu = 0.9eV$, a relaxation time $\tau = 1ps$, and refractive index $n = 1.6$. In this figure, the plasmonic mode is below the light line and $kx_{sp} >> k_0$; according to the approximation of [22], therefore it's important to note the correspondence between the two approximations (eq.3.6 and contour plot). Plasmonic modes, as observed, exist in the low THz regime, which is a characteristic of metal-like plasmons. This behavior can be traced back to Drude's model of conductivities. A more complete discussion of these dispersion relations is presented in the appendix A.1.

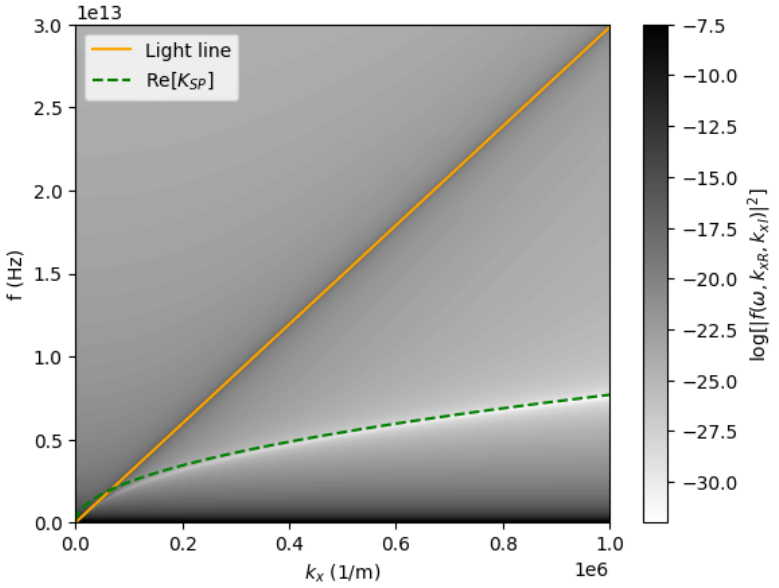

Figure **1.2**: Dispersion relation f as a function of k_x in a range from 0 to 30 THz. The orange line is the light line for $n = 1.6$. The dashed line shows the approximation taken in [22].

The next step in the calculations is the computation of propagation and decay lengths which are two important quantities to understand the behavior of electromagnetic waves or electron waves as they interact with materials. The propagation length (which we define as β) refers to the distance over which an electron wave can travel without significant scattering or energy loss. Graphene has very high electron mobility, meaning electron waves can propagate over relatively long distances without much attenuation. In fig. (**1.3**) is shown a graph of the propagation length given by the following eq. (3.10):

$$\beta = \frac{1}{2Im(k_x)}. \tag{3.10}$$

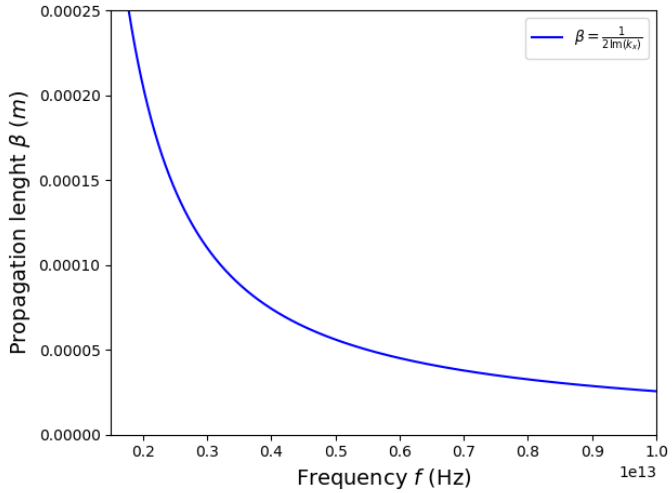

Figure **1.3**: Length propagation for a graphene-dielectric single layer with $n = 1.6$, $\mu = 1.2eV$ and $\tau = 1ps$.

As observed, the propagation length β is relatively larger at lower frequencies, indicating that the waves can travel further within the graphene before significant attenuation occurs. The curve shows that as the frequency f increases, the propagation length β decreases. This implies that the electromagnetic waves are more strongly attenuated in graphene at higher frequencies, resulting in shorter propagation lengths.

Now, we continue studying of light on spatial scales smaller than its wavelength, i. e, subwavelength optics by coupling light to matter. For 2D materials, such as graphene, phosphorene or transition metal dichalcogenides (TMDs), there exist subwavelength structures, which are those that are smaller than the wavelength of the plasmonic modes being excited. This means that the dimensions of these structures are on the order of nanometers to a few hundred nanometers, which is significantly smaller than the wavelength of visible or infrared light (which ranges from about 400 nm to 1,000 nm). Let us calculate the wavelength λ for three different frequencies $f_a = 2$ THz, $f_b = 5$ THz, and $f_c = 9$ THz. For this, we use the following relation:

$$\lambda = \frac{c}{f}, \tag{3.11}$$

where c is the speed of light and f is the frequency employed. We have $\lambda_b = 60\ \mu m$ and $\lambda_c = 33.3\ \mu m$; which are $\lambda_a \approx 1.07\beta_a$ and $\lambda_b \approx 1.16\beta_c$ respectively. More results are shown in table (3.1). In this table, we can see how the wavelengths λ's are proportional to the frequency in the two cases: with α and with β

The decay ratio α refers to the depth at which the amplitude of an electromagnetic wave decays a certain fraction of its original value as it penetrates the material. Due to the unique electronic properties of graphene, its decay length is exceptionally small, especially at high frequencies. This property makes graphene an excellent conductor of electricity, even at the nanoscale. Figure (**1.4**) shows a graph of decaying length given by:

$$\alpha = \frac{1}{Im(k_z)}. \tag{3.12}$$

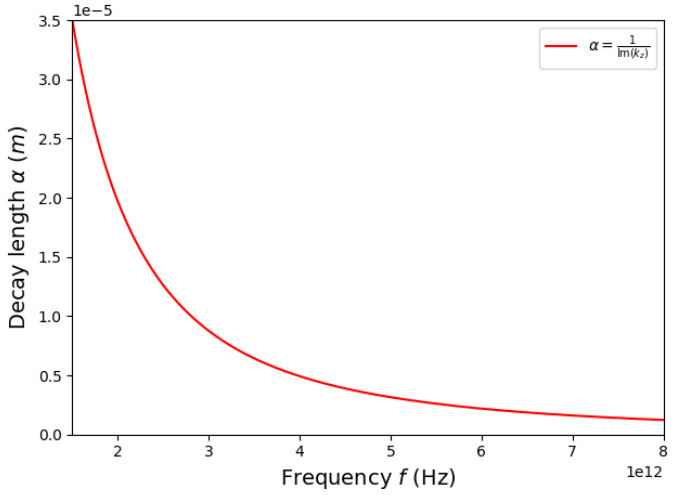

Figure **1.4**: Decay ratio α for a graphene/dielectric single-layer with $n = 1.6$, $\mu = 1.2eV$ and $\tau = 1ps$.

Table 3.1: Sub-wavelength in a graphene single-layer for three different frequencies.

	f_a $(2\ THz)$	f_b $(5\ THz)$	f_c $(9\ THz)$
λ (μm)	150	60	33.33
α (μm)	19.7	3.15	1
β (μm)	205.4	56.1	28.7
λ/α	7.61	19.01	33.33
λ/β	0.73	1.07	1.16

Next, we present two plots of the decay length α and propagation length α respectively, for a graphene single-layer varying with frequency for different carrier densities N. First, in fig.**1.5**.a), the α is plotted in meters as a function of frequency f and it's possible to observe three different color curves, these curves show that the decay length α decreases as the frequency increases. For higher carrier densities N, the decay length is longer, indicating that SPs in graphene with high carrier densities are more tightly confined to the surface and it appears that the longer decays abruptly with the other curves above a certain critical frequency. However, in fig.**1.5**b), it's possible to observe another three different color curves, which show that the propagation length β decreases with increasing frequency. For lower carrier densities N, the propagation length is shorter, meaning that SPs in graphene with lower carrier densities have shorter propagation distances before losing energy.

3.2 Plasmonic modes in phosphorene.

Similar to other 2D materials, phosphorene supports both surface plasmon polaritons (SPPs) and localized surface plasmons (LSPs). SPPs in phosphorene are influenced by its anisotropic effective mass and band structure, leading to directional propagation and polarization-dependent dispersion. LSPs, on the other hand, arise from the confinement of charge carriers within nanoscale regions of phosphorene, such as defects or edges.

Now, the analysis of plasmonic modes is started by plotting phosphorene conductivity in its two crystallography directions according to eq. (1.23). The figure (**2.6**) shows the phenomena previously mentioned, the anisotropic behavior because the Drude weight D_j where j denotes the

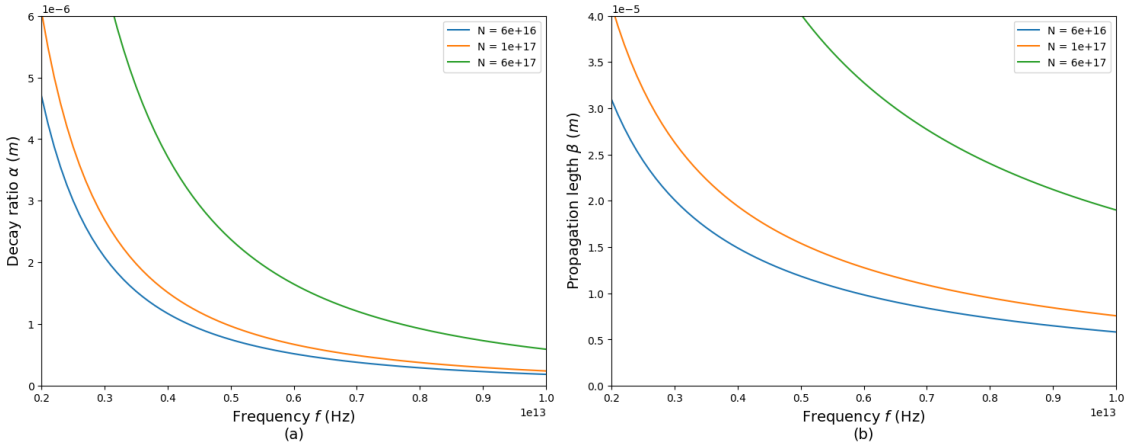

Figure **1.5**: (a) Propagation length and (b) decay ratio for a graphene single-layer with $n = 1.6$, $\tau = 1ps$ and $N = 6 \times 10^{16}, 1 \times 10^{17}$ and $6 \times 10^{17} m^{-2}$.

x (*armchair*) and y (*zigzag*) directions, which depends on the effective mass involved $m_x = 0.15m_0$ and $m_y = 0.7m_0$. In both directions (x and y), the real part of the conductivity (blue line) initially increases at low frequencies, reaches a peak, and then decreases as the frequency increases. This suggests that at lower frequencies, phosphorene absorbs more energy, but as the frequency increases, the material becomes less absorptive. The imaginary part of the conductivity (orange line) also shows a peak at low frequencies, but it decays more slowly compared to the real part as the frequency increases. This indicates that the energy storage capacity of phosphorene decreases more gradually with increasing frequency. The x-direction shows higher peak values for both, real and imaginary parts of the conductivity compared to the y-direction, indicating that phosphorene has a higher conductivity in the x-direction for the range of frequencies shown.

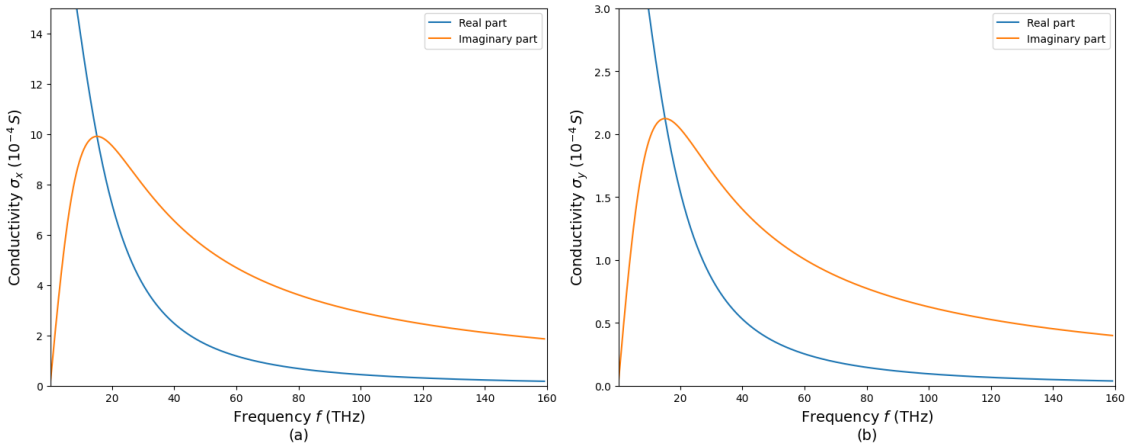

Figure **2.6**: 2D surface tensorial conductivity σ_{jj} with $\eta = 1 \times 10^{-20}\ eV$, $N = 10^{18} m^{-2}$, $\tau = 10\mu s$ and the two effective mass (a) $m_x = 0.15m_0$ and (b) $m_y = 0.7m_0$ according to [11]. In units of $S = C^2 s/kg\ m^2$.

Similar to the previous section 3.1, according to eqs. (2.24) and (1.23), the nonlinear equation for the SP dispersion relation can be solved numerically. So, we show in figure (**2.7**) the dispersion relation for a phosphorene single-layer.

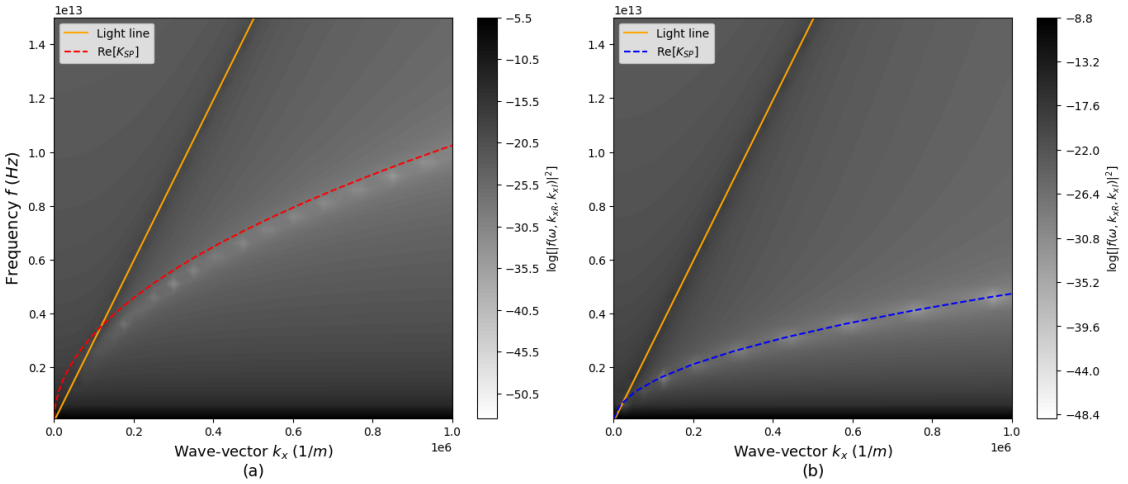

Figure **2.7**: Dispersion relations (a) and (b) for x and y directions respectively, f as function of k_x in a range from 0 to 15 THz. The orange lines are the light lines for $n = 1.6$. The dashed lines shows the approximation taken in [22].

Phosphorene, being a two-dimensional material, also exhibits unique electromagnetic properties. However, because of its anisotropic nature and electronic band structure, their propagation length β can differ depending on the direction of the electromagnetic field with respect to its crystal lattice. The fig. (**2.8**) shows two plots of the propagation length β (eq. 3.10) for both cases:

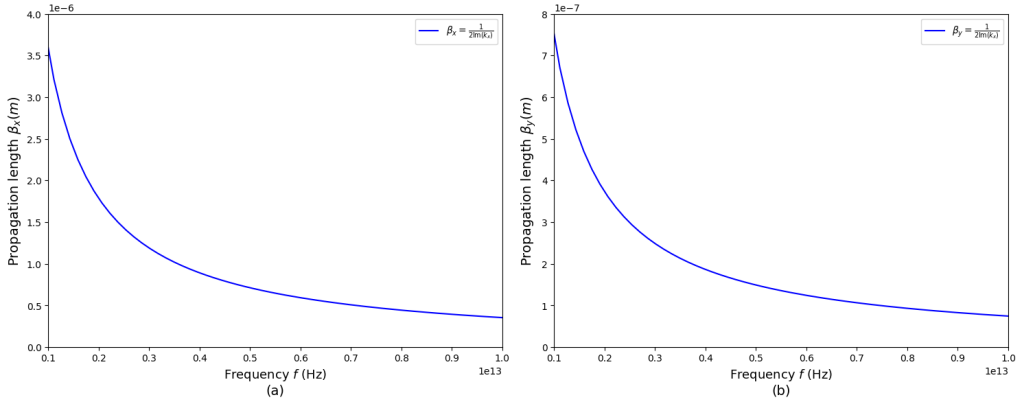

Figure **2.8**: Propagation lengths β_x and β_y for a phosphorene single layer along the (a) x-direction (*armchair*) and (b) y-direction (*zigzag*) respectively, with $n = 1.6$, $m_x = 0.15m_0$, $m_y = 0.7m_0$, $\eta = 0.1eV$ and $N = 10^{18}m^{-2}$.

As we have already seen in fig. (**2.8**), phosphorene can support the propagation of electron waves with relatively long propagation lengths (having a greater propagation along the x-direction than along y-direction.), but as f increases, the propagation decreases. Now, we see that the specific decay length α, may also be influenced by its anisotropic properties, with electron waves propagating more efficiently along a certain crystallographic direction. Fig. (**2.9**) shows two plots for the decay length α (eq. 3.12) for both directions. In the first instance, we have that the decay length (α_x and α_y) is significantly large for the first few frequencies. However, as f increases, α_x and α_y decreases abruptly to very small values. Again, in table (3.2) we present the sub-wavelength behavior in a dielectric/phosphorene single-layer configuration.

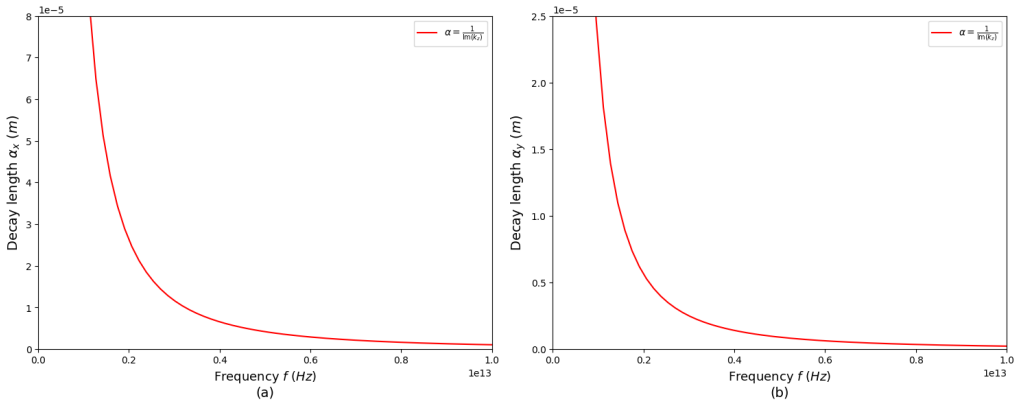

Figure **2.9**: Decay lengths (a) α_x and (b) α_y, for a phosphorene single-layer along its two directions respectively; with $n = 1.6$, $\tau = 10\mu s$ and $N = 10^{18}m^{-2}$.

Table 3.2: Sub-wavelength behavior in a phosphorene single-layer for three different frequencies.

	f_a = 2 THz	$f_b = 5THz$	f_c = 9 THz
λ (μm)	150	60	33.33
α_x (μm)	25	4	1
α_y (μm)	6	1	0.5
β_x (μm)	1.78	0.71	0.4
β_y (μm)	0.37	0.15	0.08
λ/α_x	6	15	33.33
λ/α_y	25	60	66.66
λ/β_x	84.27	84.5	83.325
λ/β_y	405.4	400	416.62

To conclude this section, in fig. (**2.10**) we show four plots representing the decay length α and propagation length β of surface plasmons in phosphorene single-layer as a function of frequency f for different carrier concentrations N in the x and y directions respectively. The properties of SPs vary significantly depending on the crystallographic direction. Each line represents three different carrier densities in the two directions (N_x and N_y). In panel (a), the subplot shows that as frequency f increases, the decay length α_x decreases. Higher carrier densities N_x lead to a slower decay in α_x. In (b), the propagation length β_x also decreases as frequency increases. Higher carrier densities N_x correspond to larger β_x values. Similarly in (c), the decay length α_y decreases with increasing frequency. The effect of N_y on α_y follows the same pattern as in the x-direction. For subplot (d), as in the case of β_x, the propagation length β_y decreases with increasing frequency, with higher carrier densities leading to larger values of β_y.

As expected, phosphorene exhibits clear anisotropy in both decay and propagation lengths, with longer distances in the x-direction compared to the y-direction. This anisotropy is consistent across all carrier concentrations. Also, decay length and propagation length, decreases as the frequency increases, which is typical for surface plasmons as higher frequencies correspond to higher energy losses. As the carrier concentration N increases, both the decay and the propagation lengths increase, meaning that lower carrier concentrations lead to shorter propagation distances for the plasmon. In phosphorene, the lengths (α and β), are grater for x-direction than y-direction which finally is a result due to the effective mass of its charge carriers, which differ due to the band structure of phosphorene. In the x-direction, the effective mass may be lower, resulting in higher conductivity. Since α and β are related to the conductivities, higher conductivities in the x-

direction lead to greater lengths.

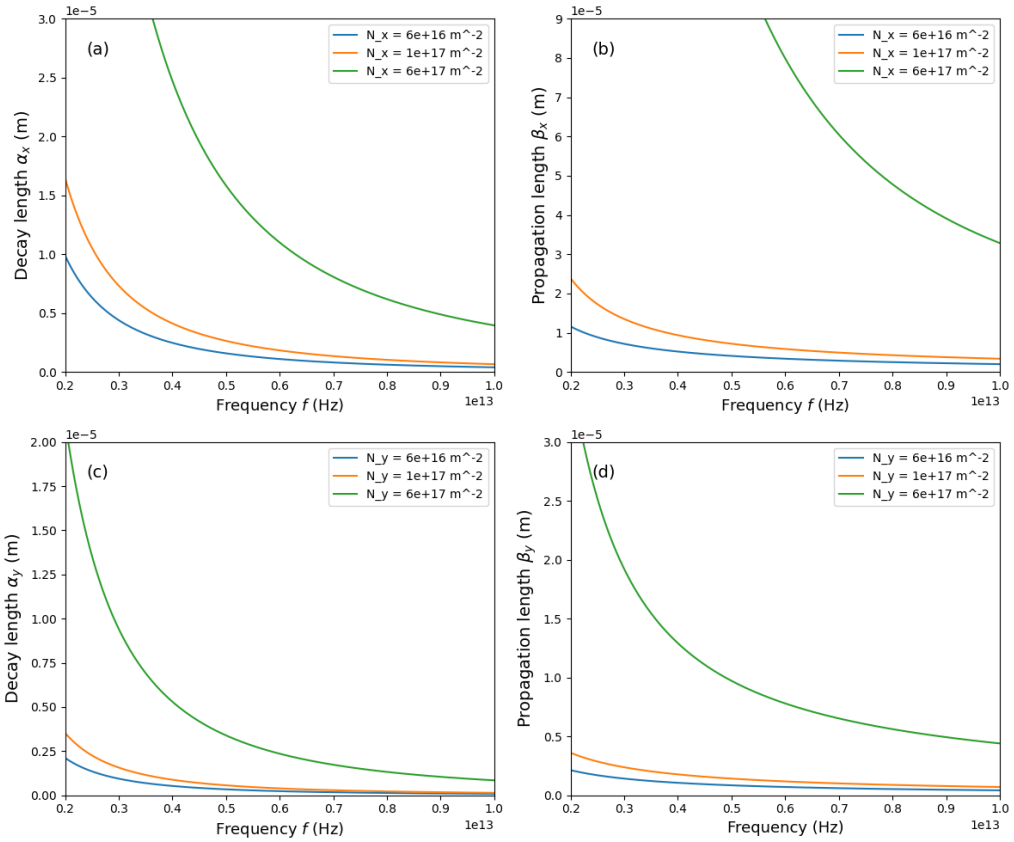

Figure **2.10**: Decay lengths and propagation lengths for a phosphorene single-layer along its two directions (a)-(b) and (c)-(d) respectively; with $n = 1.6$, $\tau = 1ps$ and spanning $N = 10^{16} - 10^{17} m^{-2}$.

3.3 Plasmonic bands in graphene and phosphorene.

Once we have demonstrated that SPs exist in graphene/phosphorene-based photonic crystals, from equation (2.42), it is possible to visualize the dispersion relations for a multilayer array via the contour plot technique. Understanding that plasmonic bands are frequency ranges in which plasmons can propagate in a material, previous reports have shown the existence of plasmonic mode coupling for TE polarization in graphene-based photonic crystals ([38]), so we want to prove that SP coupling is possible by obtaining the projected bands and extend this analysis to the case of phosphorene-based photonic crystals.

To can observe the projected TM band structure of one-dimensional periodic structure for different interlayer distances d between 2D sheets, the frequency will be presented as function of the reduced wave vector k_x. In fig.(**3.11**) we display projected bands and dispersion relation for a three phosphorene layers separated by a homogeneous dielectric medium. In panel (a), a scatter plot of $Im(K_B)$ where the green region below the light line (blue line), the region where the SP mode coupling in the PC can exist, and the red lines outline the boundaries plasmonic band, indicating the limits within which these modes can exist based on Bloch's theorem (eq. 2.56). The SP modes exist below the light line due to their nature as surface-bound waves, requiring conditions where they can be confined to the surface. On the other hand, in panel (b) we present

the same region using the contour plot technique where darker regions (below the blue light line) correspond to the dispersion relations of coupled SP modes in a three-layer structure. This result has also been reported in [38].

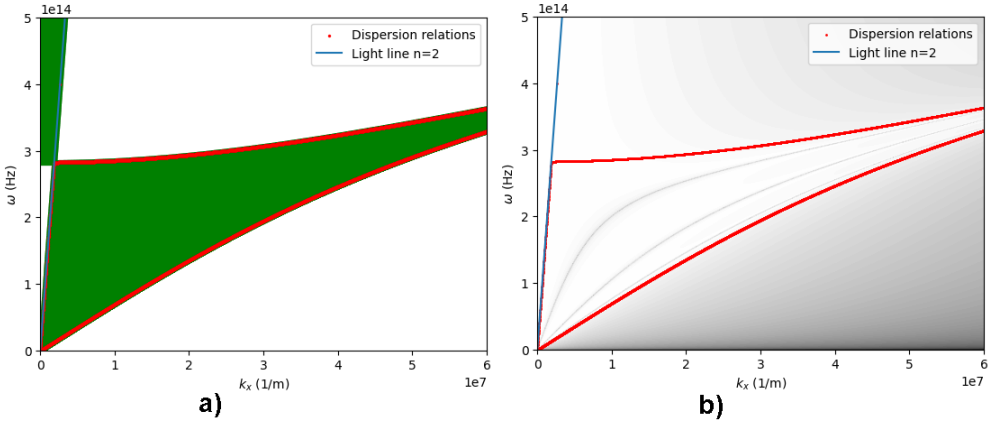

Figure **3.11**: a) Scatter plot for the plasmonic band projection zone. b) Contour plot for $N = 3$ layers of graphene. Both cases with $\tau = 10\mu s$, $\mu = 1.2eV$, $n = 2$ and $d = 50nm$.

Similar considerations are founded in fig.**3.12** for a phosphorene-based photonic crystal along the two directions. In the panels (a) and (c), scatter plots of $Im(K_B)$ are presented where the green regions are the regions where the plasmon modes can exists, all this below the light line (for the x and y directions, respectively). In panels (b) and (d), the darker regions below the light line, correspond to the coupled SP modes delimited by red lines, and in this context, the white regions outside this region would indicate areas where SP modes are forbidden.

Then, in fig.(**3.13**) the shaded (green/blue) areas correspond to the Bloch pass-band (located above the light line) and the evanescent Bloch band (located below the light line). The white areas corresponds to a metallic gap and a Bragg gap [35], this is, a frequency range where the propagation is forbidden due to constructive and destructive interference effects. In both panels a) and b), we have that blue regions below the light line, indicates the presence of SP modes in graphene-based PC and as the μ increases from 0.9 eV to 1.9 eV, the lower SP mode moves slightly upward, indicating a higher frequency for the same wave vector; also, the upper mode can shifts with the overall gap between modes becoming more distinct. This is, the SP modes in graphene shift upward in frequency with increasing doping level, reflecting tunability with external doping. Next, for both panels (c) and (d), we have that green regions below the light line, indicates the presence of SP modes in phosphorene along its two crystallographic directions. We can observe that in (c) for the x-direction (*armchair*), the modes are more spread out compared to the y-direction (*zigzag*) in (d). So, the dispersion is clearly anisotropic, with effective mass D_x showing a broader range of k_x values supporting SPs at higher frequencies, whereas D_y is more confined. This is, The SPP modes in phosphorene exhibit strong anisotropy, with the Drude weight D_x direction supporting a wider range of SPs compared to the D_y direction. This reflects phosphorene's intrinsic anisotropic electronic structure.

As previously mentioned, graphene has more isotropic behavior with tunable SP modes via doping level μ. Phosphorene, on the other hand, displays significant directional dependence, which could be advantageous in applications requiring directionally dependent plasmonic properties.

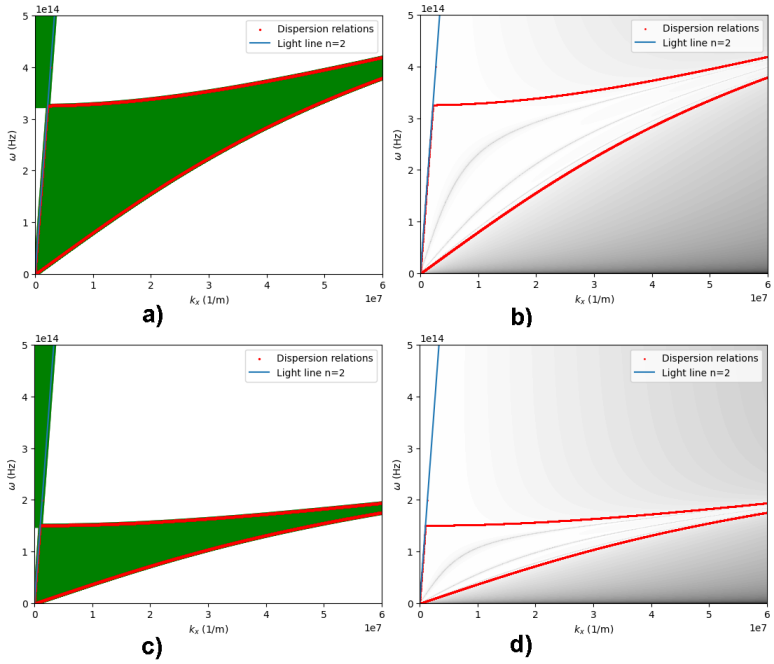

Figure **3.12**: Scatter and contour plots of the dispersion relation (2.42) for three phosphorene layers with $n = 2$, $N = 10^{18}m^{-2}$, $\tau = 10\mu s$, $d = 50nm$ in the direction a)-b) armchair and direction c)-d) zigzag.

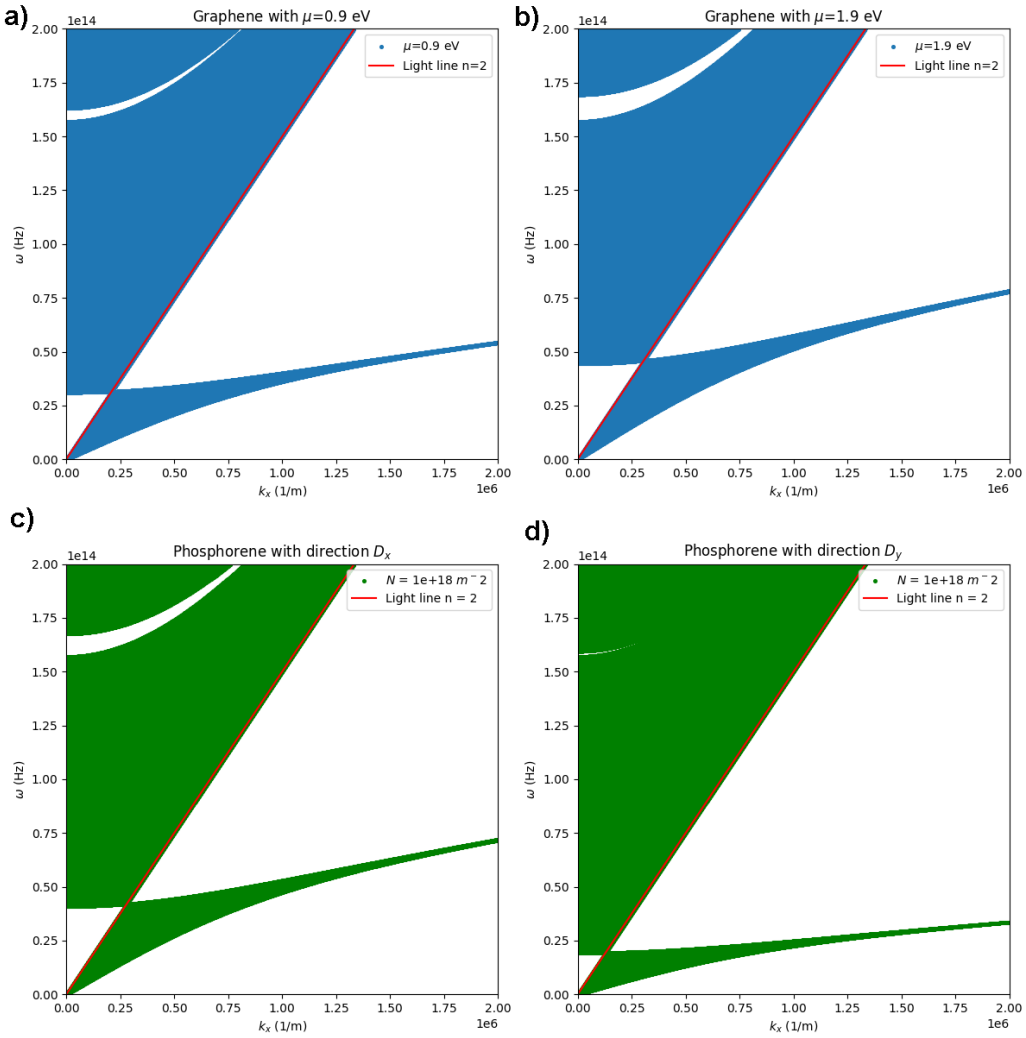

Figure **3.13**: Projection of the plasmonic band below/above the light line for a) graphene monolayer with $\mu = 0.9eV$, b) graphene monolayer with $\mu = 1.9eV$, c) phosphorene monolayer in the direction *armchair* and d) phosphorene monolayer in direction *zigzag*.

Conclusions

In this thesis we have presented a theoretical study on the propagation and coupling of surface plasmons in multilayer systems based on two-dimensional materials, such as graphene and phosphorene, when a radiation of a few THz is incident on these systems. In addition, the band structure as well as the propagation length for a one-dimensional photonic crystal were analyzed. The most important aspects of this work are presented.

In general terms, plasmonic mode coupling is possible for multilayer configurations given by dielectric-2D material (graphene or phosphorene). As shown, in figures (**1.2**) and (**2.7**), the dispersion relation of these modes is below the light-line with the TM polarization.

Starting from Bloch's theorem, we have found that for infinite structure, the coupling between plasmonic modes gives rise to plasmonic bands for both (dielectric-graphene) and for (dielectric-phosphorene) configurations.

The dispersion relation shows different behaviors for two-dimensional materials (graphene or phosphorene) and doping modulation in these materials provides the possibility to control plasmon propagation. This physical behavior was analyzed using numerical modeling with the Chebyshev polynomial technique and contour plots.

The plasmonic bands in these 2D materials offers remarkable tunability in their plasmonic responses, with graphene providing a broad frequency range and external control, and phosphorene contributing unique anisotropic properties.

One of the significant results for graphene is its high tunability through external electric fields. According to experimental results, by applying a gate voltage, we can adjust the carrier concentration N and, consequently, the plasmonic resonances and the resulting photonic band structure.

As shown in fig.**1.5**, both the decay length α and the propagation length β, decrease as the carrier density N increases. This implies that higher carrier densities in graphene result in SPs that are more confined and lose energy more rapidly. As the frequency increases, both the decay length and propagation length decrease, indicating that SPs become more confined and lose energy more quickly at higher frequencies.

Finally, the optical properties of phosphorene can be tuned by changing the number of layers or varying the orientation of the layers. This can affect the band gap and the optical response, allowing for customization of the photonic band gap.

Appendix A

Appendix

A.1 Dispersion relations for a multilayer graphene system.

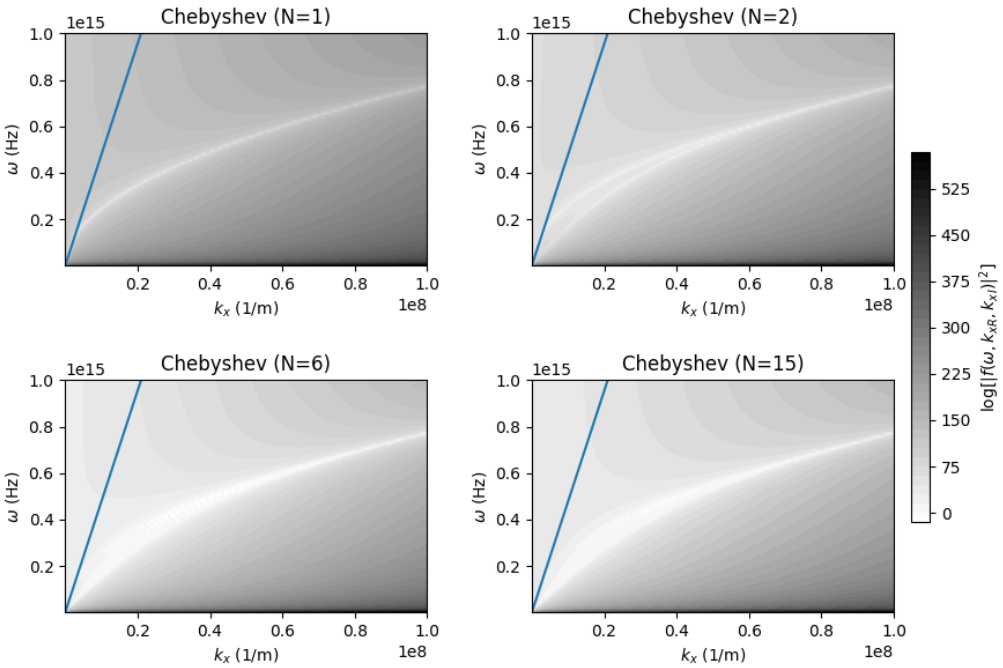

Figure **1.1**: Dispersion relations for different number of graphene layers with $n_1 = n_2 = 1.6$, $\mu = 0.9eV$, $\tau = 1ps$ using the Chebyshev relation eq. (2.42). The blue line is the light line.

From the figure (**1.1**), we can interpret that each subplot represents the frequency response of the photonic crystal structure as the number of layers N varies. The lighter areas in each subplot represent the dispersion relation of the system, showing the relationship between k_x and ω and the color intensity shows the logarithm of the squared magnitude of the technique described for eq.(3.9), indicating how waves of different frequencies and wave numbers can propagate through each interface. First, with $N = 1$, the response is relatively simple and smooth. The photonic crystal acts almost like a simple graphene/dielectric interface with just one dispersion relation. Adding a second layer, $N = 2$, introduces more structure to the response. The two-layer effect

becomes more pronounced with some regions of allowed plasmon propagation. However, from a certain critical frequency, such allowed regions seem to be confined in one and the same. As the number of layers increases, $N = 6$, the photonic band structure begins to emerge more clearly. The plot shows more complex patterns, indicating multiple regions where wave propagation is either allowed or forbidden below the light line. With $N = 15$ layers, the photonic crystal exhibits well-defined band gaps and sharp transitions in its response. This indicates strong selectivity in filtering certain frequencies and leads to more pronounced deviations from the light line, reflecting the increased complexity of the wave propagation through the multilayer system.

A.2 Dispersion relations multilayer phosphorene system.

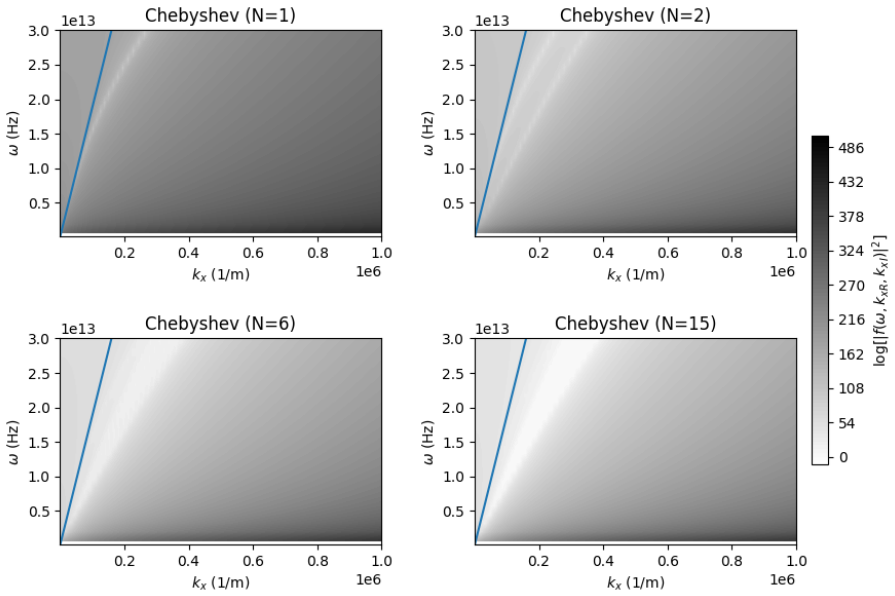

Figure **2.2**: Dispersion relations for a multilayer system of phosphorene along the x-direction (*armchair*) using the Chebyshev identity and $n = 1.6$, $d = 3\mu m$, carrier density $10^{18}m^{-2}$, $\eta = 10^{-30}J$.

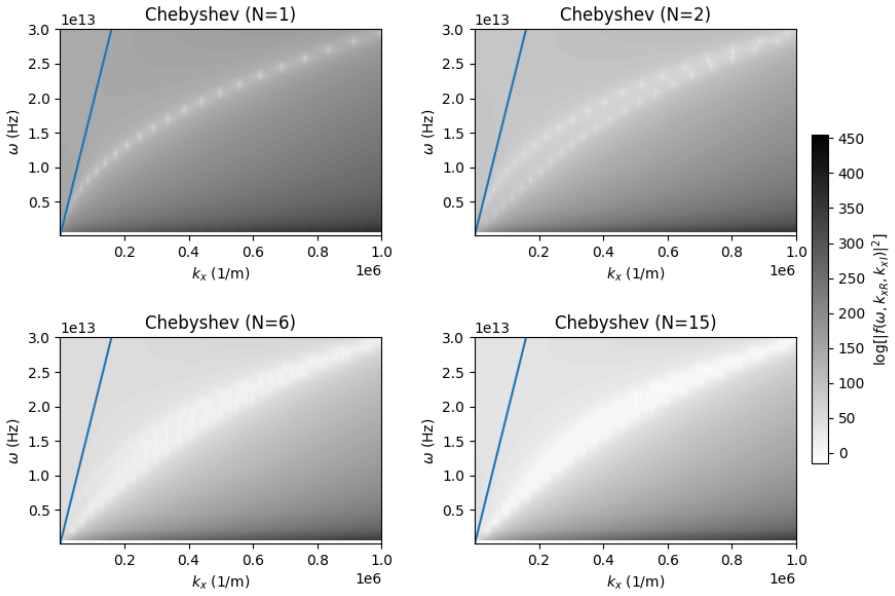

Figure **2.3**: Dispersion relations for a multilayer system of phosphorene along the y-direction (*zigzag*) using the Chebyshev identity and $n = 1.6$, $d = 3\mu m$, carrier density $10^{18}m^{-2}$, $\eta = 10^{-30}J$.

The figure effectively illustrates how increasing the number of layers in the phosphorene/dielectric photonic crystal leads to a more complex and selective frequency response. As N increases,

the crystal becomes more effective at filtering specific frequencies, demonstrating the development of a photonic band structure with well-defined band gaps.

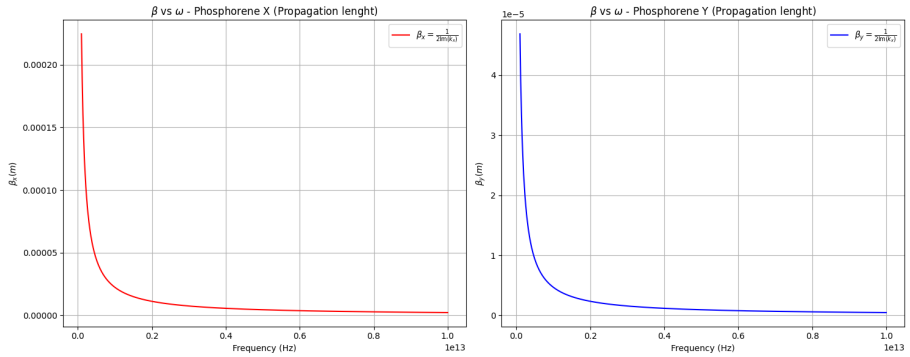

Figure **2.4**: Length propagation β for a single phosphorene layer along the x-direction (*armchair*) and y-direction (*zigzag*) using $n = 1.6$, $m_x = 0.15m_0$, $m_y = 0.7m_0$ $N = 10^{18}m^{-2}$, $\eta = 0.1eV$.

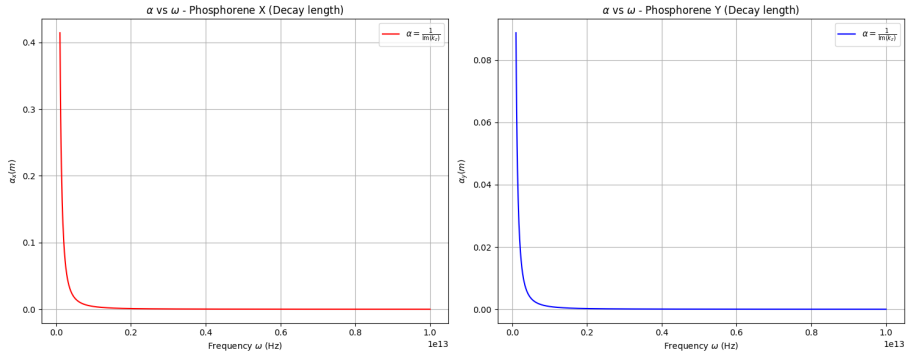

Figure **2.5**: Decay length α for a single phosphorene layer along the x-direction (*armchair*) and y-direction (*zigzag*) using $n = 1.6$, $m_x = 0.15m_0$, $m_y = 0.7m_0$ $N = 10^{18}m^{-2}$, $\eta = 0.1eV$.

Listing A.1: Python code for the dispersion relation and contour plot of Eq. (3.8)

```
# -*- coding: utf-8 -*-
"""Prueba05Dic.ipynb

Automatically generated by Colab.

Original file is located at
    https://colab.research.google.com/drive/1bL1FbxXxS-
        FAWTTPYbD9wHQdcHdpSlhw
"""

import numpy as np
import matplotlib.pyplot as plt

# constantes
hbar = 1.0545e-34
tau = 1e-12
e = 1.6021e-19
mu = 0.9 * e     #0.9eV
```

```
c = 2.9979e8
n1 = 1.6
n2 = 1.6
epsilon_0 = 8.8546e-12
epsilon_1 = n1**2
epsilon_2 = n2**2

# Se define la conductividad sigma
def sigma(omega):
    return (1j * e**2 * mu) / (np.pi * hbar**2 * (omega + 1j/tau))

# Se define la funci n f
def f(omega, kx, ky):
    term1 = epsilon_1 / np.sqrt(((omega**2 / c**2) * epsilon_1 - (kx + 1j*
        ky)**2))
    term2 = epsilon_2 / np.sqrt(((omega**2 / c**2) * epsilon_2 - (kx + 1j*
        ky)**2))
    numerador = sigma(omega)
    denominador = epsilon_0 * omega
    return term1 + term2 + numerador / denominador

# Definici n de la funci n ksp (Choon)
def ksp(omega):
    return ((n1**2 + n2**2) * (1j * omega * epsilon_0)) / sigma(omega)


# Define el rango de valores para omega y kx
frequencies = np.linspace(0.1e12, 10e13, 1000)  # Valores de f en rad/s
    pasando por los THz
# Calcular omega usando la relaci n omega = 2 * pi * f
omega = 2 * np.pi * frequencies
kx_values = np.linspace(0.1, 1e6, 1000)

# Se crea una cuadr cula de valores para omega y kx
omega_grid, kx_grid = np.meshgrid(omega, kx_values)

# Se crea una cuadr cula de valores para f y kx
f_grid, kx_grid = np.meshgrid(frequencies, kx_values)

# Se eval a la funci n para las omega,kx y ky constante
z = f(omega_grid, kx_grid, ky=0)

# Se aplica el log(f^2)
w = (abs(z))**2
h = np.log(w)

# Se eval a ksp en funci n de la frecuencia angular omega
m =  ksp(omega)

# Par metros para la l nea de luz 1 w = c*kx/n1
light_line1 = (kx_values * c)//(n1 * 2 * np.pi)

# Par metros para la l nea de luz 2 w = c*kx
light_line2 = (kx_values * c)//(n2 * 2 * np.pi)

# Se crea la gr fica de contorno sobre un plano 2D
```

```
plt.contourf(kx_grid, f_grid, h, levels=100, cmap='binary')
plt.plot(kx_values, light_line1, label='Light line', color='orange')
#plt.plot(light_line2, kx_values, label='L nea de luz n2')
plt.plot(np.real(m), frequencies, label='Re[$K_{SP}$]',linestyle='--',
    color='g')
plt.ylabel('f (Hz)')
plt.xlabel('$k_x$ (1/m)')
plt.xlim(0,1e6)
plt.ylim(0,3e13)
plt.colorbar(label='$\log[|f( \omega, {k_x}_R, {k_x}_I)|^2 ]$')
plt.legend(loc='upper left')
plt.show()
```

Bibliography

[1] A. Geim and K.S. Novoselov. The rise of graphene. *Nature materials*, 6:183–91, 04 2007.

[2] A. H. Castro Neto, F. Guinea, N. M. R. Peres, K. S. Novoselov, and A. K. Geim. The electronic properties of graphene. *Rev. Mod. Phys.*, 81:109–162, Jan 2009.

[3] Pulickel Ajayan, Philip Kim, and Kaustav Banerjee. Two-dimensional van der Waals materials. *Physics Today*, 69(9):38–44, 09 2016.

[4] Line Jelver and Joel D. Cox. Nonlinear plasmonics in nanostructured phosphorene. *ACS Nano*, 17(20):20043–20052, 2023. PMID: 37791979.

[5] Han Liu, Adam T. Neal, Zhen Zhu, Zhe Luo, Xianfan Xu, David Tománek, and Peide D. Ye. Phosphorene: An unexplored 2d semiconductor with a high hole mobility. *ACS Nano*, 8(4):4033–4041, 2014. PMID: 24655084.

[6] Likai Li, Yijun Yu, Guo Jun Ye, Qingqin Ge, Xuedong Ou, Hua Wu, Donglai Feng, Xian Hui Chen, and Yuanbo Zhang. Black phosphorus field-effect transistors. *Nature Nanotechnology*, 9(5):372–377, March 2014.

[7] Meysam Akhtar, George Anderson, Rong Zhao, Adel Alruqi, Joanna E Mroczkowska, Gamini Sumanasekera, and Jacek B Jasinski. Recent advances in synthesis, properties, and applications of phosphorene. *npj 2D Materials and Applications*, 1(1):5, 2017.

[8] Jingzhi Zhang and Hong Zhang. Tuning of the optical properties of monolayer blue phosphorene. *Plasmonics*, 16, 02 2021.

[9] Alexandra Carvalho, Min Wang, Xi Zhu, Aleksandr Rodin, Haibin Su, and Antonio Castro Neto. Phosphorene: From theory to applications. *Nature Reviews Materials*, 1:16061, 08 2016.

[10] Tony Low, Rafael Roldán, Han Wang, Fengnian Xia, Phaedon Avouris, Luis Martín Moreno, and Francisco Guinea. Plasmons and screening in monolayer and multilayer black phosphorus. *Phys. Rev. Lett.*, 113:106802, Sep 2014.

[11] Desalegn Tadesse Debu, Stephen Bauman, David French, Hugh Churchill, and Joseph Herzog. Tuning infrared plasmon resonance of black phosphorene nanoribbon with a dielectric interface. *Scientific Reports*, 8, 02 2018.

[12] Kostya S Novoselov, Andre K Geim, Sergei V Morozov, De-eng Jiang, Yanshui Zhang, Sergey V Dubonos, Irina V Grigorieva, and Alexandr A Firsov. Electric field effect in atomically thin carbon films. *science*, 306(5696):666–669, 2004.

[13] K. S. Novoselov, A. K. Geim, S. V. Morozov, D. Jiang, M. I. Katsnelson, I. V. Grigorieva, S. V. Dubonos, and A. A. Firsov. Two-dimensional gas of massless dirac fermions in graphene. *Nature*, 438(7065):197–200, November 2005.

[14] JS Gomez-Diaz, C Moldovan, S Capdevila, J Romeu, LS Bernard, A Magrez, AM Ionescu, and Julien Perruisseau-Carrier. Self-biased reconfigurable graphene stacks for terahertz plasmonics. *Nature communications*, 6(1):6334, 2015.

[15] Daria Smirnova, Pavel Buslaev, Ivan Iorsh, Ilya V. Shadrivov, Pavel A. Belov, and Yuri S. Kivshar. Deeply subwavelength electromagnetic tamm states in graphene metamaterials. *Phys. Rev. B*, 89:245414, Jun 2014.

[16] L. A. Tepanecatl Fuentes, I. Fuentecilla-Carcamo, J. M. Gutierrez-Villarreal, Jorge A. Gaspar-Armenta, M. A. Palomino-Ovando, and G. Hernández-Cocoletzi. Effective plasma frequency in tunable THz reflectors based on graphene and phosphorene. *Journal of Applied Physics*, 129(21):213103, 06 2021.

[17] C. Rebolledo Espinoza, D.A. Ryndyk, A. Dianat, R. Gutierrez, and G. Cuniberti. First principles study of field effect device through van der waals and lateral heterostructures of graphene, phosphorene and graphane. *Nano Materials Science*, 4(1):52–59, 2022. Special issue on Graphene and 2D Alternative Materials.

[18] M. Saifur Rahman, Md. Shamim anower, and Lway Faisal Abdulrazak. Utilization of a phosphorene-graphene/tmdc heterostructure in a surface plasmon resonance-based fiber optic biosensor. *Photonics and Nanostructures - Fundamentals and Applications*, 35:100711, 2019.

[19] M. Saifur Rahman, Md. Shamim Anower, Lway Faisal Abdulrazak, and Md. Maksudur Rahman. Modeling of a fiber-optic surface plasmon resonance biosensor employing phosphorene for sensing applications. *Optical Engineering*, 58(3):037103, 2019.

[20] Ryogo Kubo. Statistical-mechanical theory of irreversible processes. i. general theory and simple applications to magnetic and conduction problems. *Journal of the Physical Society of Japan*, 12(6):570–586, 1957.

[21] K. Ziegler. Robust transport properties in graphene. *Phys. Rev. Lett.*, 97:266802, Dec 2006.

[22] Choon How Gan. Analysis of surface plasmon excitation at terahertz frequencies with highly-doped graphene sheets via attenuated total reflection. *Applied Physics Letters*, 101, 03 2013.

[23] F. Ramos-Mendieta, J. A. Hernández-López, and M. Palomino-Ovando. Transverse magnetic surface plasmons and complete absorption supported by doped graphene in Otto configuration. *AIP Advances*, 4(6):067125, 06 2014.

[24] Stefan A Maier et al. *Plasmonics: fundamentals and applications*, volume 1. Springer, 2007.

[25] John David Jackson. *Classical electrodynamics; 2nd ed.* Wiley, New York, NY, 1975.

[26] P. Yeh. *Optical Waves in Layered Media*. Wiley Series in Pure and Applied Optics. Wiley, 2005.

[27] Felix Bloch. Über die quantenmechanik der elektronen in kristallgittern. *Zeitschrift für Physik*, 52:555–600, 1929.

[28] C. Kittel, P. McEuen, and John Wiley & Sons. *Introduction to Solid State Physics*. John Wiley & Sons, 2005.

[29] J.D. Joannopoulos, S.G. Johnson, J.N. Winn, and R.D. Meade. *Photonic Crystals: Molding the Flow of Light - Second Edition*. Princeton University Press, 2011.

[30] Audrey Moores and Frédéric Goettmann. The plasmon band in noble metal nanoparticles: an introduction to theory and applications. *New J. Chem.*, 30:1121–1132, 2006.

[31] Chunlian Cen, Yubin Zhang, Xifang Chen, Hua Yang, Zao Yi, Weitang Yao, Yongjian Tang, Yougen Yi, Junqiao Wang, and Pinghui Wu. A dual-band metamaterial absorber for graphene surface plasmon resonance at terahertz frequency. *Physica E: Low-dimensional Systems and Nanostructures*, 117:113840, 2020.

[32] Amir Madani and Samad Roshan Entezar. Optical properties of one-dimensional photonic crystals containing graphene sheets. *Physica B: Condensed Matter*, 431:1–5, 2013.

[33] P. Wachsmuth, R. Hambach, G. Benner, and U. Kaiser. Plasmon bands in multilayer graphene. *Phys. Rev. B*, 90:235434, Dec 2014.

[34] Barun Ghosh, Piyush Kumar, Anmol Thakur, Yogesh Singh Chauhan, Somnath Bhowmick, and Amit Agarwal. Anisotropic plasmons, excitons, and electron energy loss spectroscopy of phosphorene. *Phys. Rev. B*, 96:035422, Jul 2017.

[35] H. Hajian, A. Soltani-Vala, and M. Kalafi. Characteristics of band structure and surface plasmons supported by a one-dimensional graphene-dielectric photonic crystal. *Optics Communications*, 292:149–157, 2013.

[36] I. Fuentecilla-Carcamo, M. Palomino-Ovando, and F. Ramos-Mendieta. One dimensional graphene based photonic crystals: Graphene stacks with sequentially-modulated doping for photonic band gap tailoring. *Superlattices and Microstructures*, 112:46–56, 2017.

[37] P.A.D. Goncalves and N.M.R. Peres. *An Introduction To Graphene Plasmonics*. World Scientific Publishing Company, 2016.

[38] I. Fuentecilla-Carcamo, J.A. Gaspar-Armenta, M.A. Palomino-Ovando, Y. Panecatl-Bernal, L.A. Tepanecatl Fuentes, and F. Ramos-Mendieta. Plasmonic mode coupling in graphene-based photonic crystals. *Superlattices and Microstructures*, 139:106396, 2020.